

Kibble-Zurek scaling of the superfluid-supersolid transition in an elongated dipolar gas

Wyatt Kirkby^{1,2}, Hayder Salman^{3,4}, Thomas Gasenzer^{1,5} and Lauriane Chomaz²

¹Kirchhoff-Institut für Physik, Universität Heidelberg, Im Neuenheimer Feld 227, 69120 Heidelberg, Germany

²Physikalisches Institut, Universität Heidelberg, Im Neuenheimer Feld 226, 69120 Heidelberg, Germany

³School of Engineering, Mathematics, and Physics, University of East Anglia, Norwich Research Park, Norwich NR4 7TJ, United Kingdom

⁴Centre for Photonics and Quantum Science, University of East Anglia, Norwich Research Park, Norwich NR4 7TJ, United Kingdom

⁵Institut für Theoretische Physik, Universität Heidelberg, Philosophenweg 16, 69120 Heidelberg, Germany



(Received 27 November 2024; accepted 15 May 2025; published 11 June 2025)

We simulate interaction quenches crossing from a superfluid to a supersolid state in a dipolar quantum gas of ¹⁶⁴Dy atoms, trapped in an elongated tube with periodic boundary conditions, via the extended Gross-Pitaevskii equation. A freeze-out time is observed through a delay in supersolid formation after crossing the critical point. We compute the density-density correlations at the freeze-out time and extract the frozen correlation length for the solid order. An analysis of the freeze-out time and correlation length versus the interaction quench rate allows us to extract universal exponents corresponding to the relaxation time and correlation length based on predictions of the Kibble-Zurek mechanism. Over several orders of magnitude, clear power-law scaling is observed for both the freeze-out time and the correlation length, and the corresponding exponents are compatible with predictions based on the excitation spectrum calculated via Bogoliubov theory. Defects due to independent local breaking of translational symmetry, contributing to globally incommensurate supersolid order, are identified, and their number at the freeze-out time is found to also scale as a power law. Our results support the hypothesis of a continuous transition whose universality class remains to be determined but appears to differ from that of the (1 + 1)-dimensional XY model.

DOI: [10.1103/x51r-vdyf](https://doi.org/10.1103/x51r-vdyf)

I. INTRODUCTION

Spontaneous breaking of translational symmetry in a superfluid can result in an exotic phase of matter that maintains phase coherence while exhibiting periodic crystalline order: a supersolid [1–6]. Supersolids have been realized in ultracold quantum gases using spin-orbit-coupled systems [7,8] and with strongly magnetic dipolar atoms [9–11]. In the latter, the transition to a solid phase can be achieved either by starting from a thermal gas and quenching the temperature [11–13] or starting from a superfluid and changing the interparticle interaction strength [9–11]. Furthermore, depending on the system parameters and geometry, the quantum phase transition from superfluid to supersolid has been found to be either continuous or discontinuous [14–20]; however, the exact critical behavior and the corresponding universality classes of these transitions have yet to be determined.

When tuning a control parameter λ towards its critical value λ_c at a continuous phase transition, characteristic scales diverge following universal power laws, defining the critical behavior at the phase transition and being independent of the microscopic details. Precisely, the correlation length ξ and relaxation time τ diverge as $\xi(\lambda) \sim |\lambda - \lambda_c|^{-\nu}$ and $\tau(\lambda) \sim \xi^z \sim |\lambda - \lambda_c|^{-\nu z}$, respectively, with ν and z the critical exponents

determined by the universality class of the transition [21–23], see Figs. 1(a) and 1(b).

The theory of the Kibble-Zurek mechanism (KZM) [24–27] provides a framework for understanding symmetry breaking in a dynamical setting. It predicts that critical slowing down and the divergence of both the characteristic length and time scales prevent the system from preserving an instantaneous parametric equilibrium state in quenches across continuous phase transitions. More specifically, in a quench of the control parameter λ , such as $\lambda - \lambda_c \propto t/\tau_Q$, the relaxation time $\tau(t)$ rapidly increases and surpasses the time left to the transition at time $t = -\hat{t} = -\tau(\hat{t})$, so-called freezing-out time. For $t > -\hat{t}$, adiabaticity is broken, the system becomes frozen, and fluctuations present remain embedded in the system until it unfreezes, which similarly occurs at a certain time after crossing the critical point, namely for $t > \hat{t}$. During the freeze-out period and as adiabaticity is lost, domains with distinct local order roughly of size $\hat{\xi} = \xi(\hat{t})$ persist.

Based on the equilibrium scaling laws above, the freeze-out time and domain size for a linear quench of the order parameter at a constant rate τ_Q scale as

$$\hat{t} \propto \tau_Q^{z\nu/(1+z\nu)} \equiv \tau_Q^{\zeta_{KZ}} \quad \text{and} \quad \hat{\xi} \propto \tau_Q^{\nu/(1+z\nu)} \equiv \tau_Q^{\nu_{KZ}}, \quad (1)$$

respectively, see Figs. 1(a) and 1(b). Higher quench rates lead to the breakdown of adiabaticity at lower values of \hat{t} (faster supersolid formation) and correspondingly lower $\hat{\xi}$ (smaller domain sizes). The boundaries of these domains can be identified as defects, corresponding to sudden changes in the value of the order parameter in space, and separating

Published by the American Physical Society under the terms of the Creative Commons Attribution 4.0 International license. Further distribution of this work must maintain attribution to the author(s) and the published article's title, journal citation, and DOI.

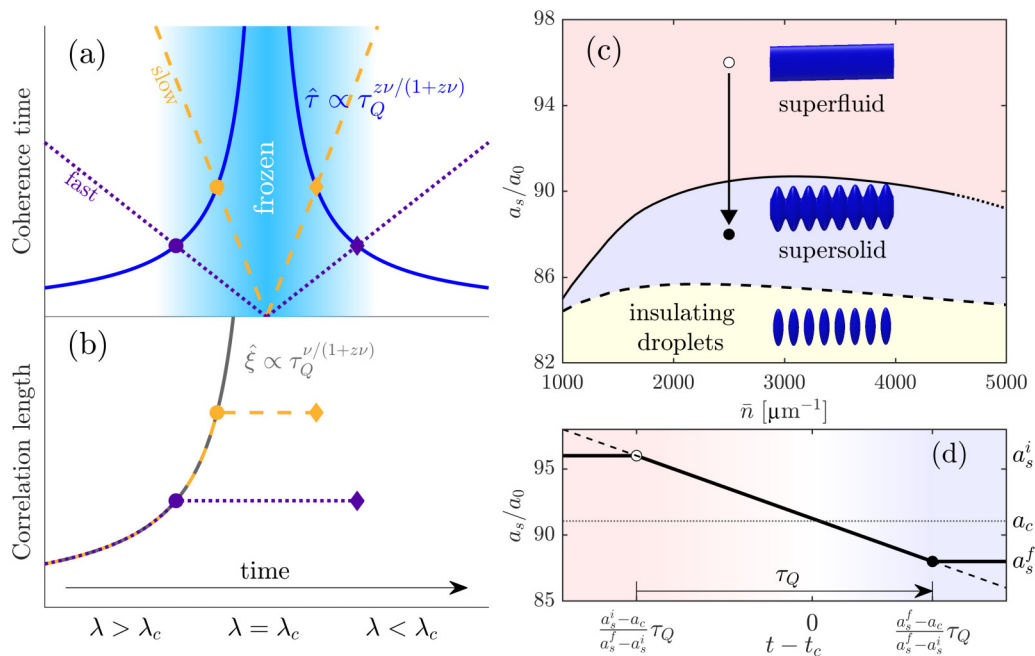


FIG. 1. The KZM in quenches across the superfluid-supersolid transition. Panel (a) depicts the typical KZM schematic. The coherence time τ (blue curve) diverges at the critical point. Two quench ramps linear in time t (slow: green dashed, fast: yellow dotted) of a control parameter are indicated. The freeze-out time \hat{t} occurs when $|t|$ crosses τ . Panel (b) depicts the diverging correlation length ξ (gray solid curve), which becomes frozen at $\hat{\xi}$, as depicted here for the two ramps of panel (a). Panel (c) shows the phase diagram for the elongated dipolar system, with a continuous (solid line) or discontinuous (dotted line) transition from superfluid to supersolid phases, and a crossover from supersolid to insulating droplet (dashed line). Sample isodensity surfaces for each phase are shown. The start (empty circle) and end points (filled circle) for the quenches considered in this paper are indicated. The quench protocol is shown in panel (d), with the total quench time τ_Q varying throughout the paper. Most quenches follow the solid line, while for extremely fast quenches ($\tau_Q < 10$ ms), the dashed line is followed.

independent causally disconnected regions where the symmetry is independently broken. By studying the scaling of the freeze-out time, domain size, or remaining defects, one can extract critical scaling exponents of the underlying transition and thereby probe the transition universality class.

The KZM has been successfully applied to a wide range of systems [27–29]. This is in particular true for quantum gases where it has been studied both theoretically [30–44], and experimentally, via temperature quenches [45–58] and in quantum phase transitions [51,59–67]. The transition to supersolid states offers a new context, where the KZM could be induced, and its study may yield new insights into the nature of the underlying transitions.

In this paper, we study the KZM in the context of a continuous quantum phase transition from a superfluid to a one-dimensional supersolid in an elongated tube at a fixed density by tuning the s -wave scattering length a_s , see Fig. 1(c). We cross the transition at a finite rate and examine the scalings of the characteristic scales with the quench rate. In Sec. II, we present the equations of motion for the dipolar gas, illustrate how the ground state phase diagram is calculated, and present details of our dynamical simulations. Sections III D and III C present our observations for power-law scalings of the freeze-out time, domain size, and defect densities, respectively, along with the corresponding scaling exponents. In Sec. III D, based on these KZM scalings, we extract the critical exponents ν and z of the superfluid-to-supersolid transition and comment on its universality class.

II. MODEL

A. Equations of motion

To simulate the dipolar gas, we begin with the extended Gross-Pitaevskii equation (eGPE),

$$i\hbar \frac{\partial \Psi(\mathbf{r}, t)}{\partial t} = \left[-\frac{\hbar^2 \nabla^2}{2m} + V(\mathbf{r}) + g|\Psi(\mathbf{r}, t)|^2 + \gamma_{\text{QF}}|\Psi(\mathbf{r}, t)|^3 + \int d^3 r' U_{\text{dd}}(\mathbf{r} - \mathbf{r}') |\Psi(\mathbf{r}', t)|^2 \right] \Psi(\mathbf{r}, t), \quad (2)$$

for atomic species with mass m and contact interaction strength $g = 4\pi\hbar^2 a_s/m$ for an s -wave scattering length a_s . We assume the system is harmonically trapped along two directions via $V(\mathbf{r}) = \frac{1}{2}m(\omega_y^2 y^2 + \omega_z^2 z^2)$ while the x direction is untrapped. The dipole-dipole interaction (DDI) is given by $U_{\text{dd}}(\mathbf{r}) = \mu_0 \mu_m^2 (1 - 3\cos^2 \theta)/(4\pi|\mathbf{r}|^3)$ where θ is the angle between \mathbf{r} and the z axis along which the dipoles are polarized. Each atom has a magnetic moment μ_m , and μ_0 is the vacuum permeability. The supersolid phase is protected from collapse [68–70] by the beyond-mean-field quantum fluctuations term proportional to $\gamma_{\text{QF}} = \frac{32}{3}g(a_s^3/\pi)^{1/2}Q_5(\epsilon_{\text{dd}})$ [71,72], with $Q_5(\epsilon) = \text{Re}\{\int_0^1 du [1 + (3u^2 - 1)\epsilon]^{5/2}\}$, where $\text{Re}\{\cdot\}$ denotes the real part, $\epsilon_{\text{dd}} = a_{\text{dd}}/a_s$, and $a_{\text{dd}} = \mu_0 \mu_m^2/(12\pi\hbar^2)$. The wavefunction is normalized to the total particle number

$N = \int d^3r |\Psi(\mathbf{r})|^2$. Note that the eGPE does not account for the quantum fluctuations in a fully self-consistent manner (as the higher-order diagrams are taken into account nondynamically). The resulting equation of motion [Eq. (2)] is thereby again mean-field-like.

We use a reduced three-dimensional (3D) model introduced in Refs. [15,73,74], which assumes that the wavefunction $\Psi(\mathbf{r})$ is separable,

$$\Psi(\mathbf{r}) = \varphi(y, z)\psi(x, t), \quad (3)$$

with the radial wavefunction

$$\varphi(y, z) = \frac{1}{\ell\sqrt{\pi}} \exp\left[-\frac{\eta y^2 + z^2/\eta}{2\ell^2}\right], \quad (4)$$

where ℓ and η are variational parameters corresponding to the $1/e$ condensate width and ellipticity (due to magnetostriction), respectively, obtained via minimization of the eGPE in imaginary time. The reduced eGPE then reads

$$\begin{aligned} i\hbar \frac{\partial \psi(x, t)}{\partial t} = & \left[-\frac{\hbar^2}{2m} \frac{\partial^2}{\partial x^2} + \mathcal{E}_\perp + \frac{g}{2\pi\ell^2} |\psi(x, t)|^2 \right. \\ & + \frac{2\gamma_{\text{QF}}}{5\pi^{3/2}\ell^3} |\psi(x, t)|^3 \\ & \left. + \int dx' U^{\text{1D}}(x-x') |\psi(x', t)|^2 \right] \psi(x, t), \quad (5) \end{aligned}$$

where $\mathcal{E}_\perp = \hbar^2(\eta + 1/\eta)/(4m\ell^2) + m\ell^2(\omega_y^2/\eta + \eta\omega_z^2)/4$, and where we have defined the effective quasi-one-dimensional (quasi-1D) DDI $U^{\text{1D}}(x-x')$, which, for dipoles polarized along the z axis, has the Fourier representation, $\tilde{U}^{\text{1D}}(k) = \mu_0\mu_m^2[4 - 2\eta - 3\sqrt{\eta}k^2\ell^2 e^{\sqrt{\eta}k^2\ell^2/2} \text{Ei}(-\sqrt{\eta}k^2\ell^2/2)]/[12\pi\ell^2(1+\eta)]$, where $\text{Ei}(k)$ is the exponential integral, and k is the conjugate momentum to the x coordinate. We will focus on an elongated gas of ^{164}Dy , with $\mu_m = 9.93\mu_B$ in terms of the Bohr magneton μ_B , in an elongated tube with trapping frequencies $\{\omega_y, \omega_z\} = 2\pi \times \{150, 150\}$ Hz. The eGPE results in unitary time evolution, conserving total atom number. However, due to the fact that we are quenching the scattering length, total energy is not conserved over the course of the dynamics.

B. Ground states

Prior to performing any quenches, we consider the ground state properties of the system. In order to determine the ground state of the system, and therefore the phase diagram, we perform an imaginary-time evolution of the reduced eGPE given in Eq. (5). We apply a split-step Fourier algorithm with an adaptive time step. For the ground state and dynamic simulations (next section), a spatial grid of approximately $0.04 \mu\text{m}$ is selected, such that there are always approximately 5–8 grid points per healing length, depending on the location in the phase diagram. By evaluating the long-range interaction term in momentum space, it is computationally efficient to simulate a single unit cell of the supersolid crystal (for ground-state calculations only) and allow alias Fourier copies of the simulation cell to self-interact [75]. By minimizing the energy per particle with respect to the variational parameters ℓ , η , and

primitive unit cell length L_{uc} , it becomes possible to determine the ground state at each point in the phase diagram.

The phase diagram for this system is sketched in Fig. 1(c), cf. Refs. [15,16]. In order to characterize the phases of the system, we make use of Leggett's estimate on the upper bound of the superfluid fraction [5],

$$f^s = \frac{L^2}{N} \left[\int dx \left(\int dy dz |\Psi|^2 \right)^{-1} \right]^{-1}, \quad (6)$$

where $L = \int dx$. A value of $f^s = 1$ indicates the uniform superfluid regime, $0.1 < f^s < 1$ for the supersolid phase, and $f^s \leq 0.1$ corresponds to insulating droplets. The boundary to the latter is not captured by our eGPE simulation, and the threshold choice of 0.1 is arbitrary, yet the details of this transition are irrelevant to the present work. We will be using f^s as an order parameter for the superfluid-supersolid transition. It should be remarked that the expression in Eq. (6) corresponds strictly to an estimate of the *upper* bound of the superfluid fraction. However, a lower bound has also been derived [76], and in the case of a 1D system where the modulation exists along one direction (the case we consider here), the two bounds are exactly equal. Using the density modulation contrast $\mathcal{C} = [\max(n) - \min(n)]/[\max(n) + \min(n)]$ as an order parameter instead of f^s was found to give similar results.

The order of the transition depends on the linear density [15,16,77] (see also the experiment in Ref. [78]), $\bar{n} = N/L$, and is discontinuous at both low ($\bar{n} \lesssim 800 \mu\text{m}^{-1}$) and high ($\bar{n} \gtrsim 4500 \mu\text{m}^{-1}$) densities. In the intermediate regime, the transition is continuous: the ground state's modulation emerges smoothly, precisely when the roton mode, calculated with Bogoliubov theory, becomes unstable in the dispersion relation. In this way, the continuous phase transition can be pinpointed precisely, whereas in the first-order regime, a bistable region emerges where the true ground state is already modulated, even though the roton has not yet fully softened. In this paper, as a first study of the KZM applied to dipolar supersolids, we restrict our quenches to an intermediate regime in which the transition is expected to be continuous, taking $\bar{n} = 2500 \mu\text{m}^{-1}$, for which the superfluid-supersolid transition is found to occur at $a_s = a_s^{\text{(GS)}} \approx 90.5a_0$.

C. Ramp into the supersolid phase

In this work, the initial state is selected to be the ground state of the uniform superfluid regime at $a_s^i = 96a_0$. Thermal noise at a temperature of $T = 20$ nK is then added (see Appendix A for details), typically adding approximately 3%–5% excited atoms, and allowed to equilibrate for 10 ms. The initial noise is crucial to trigger the dynamics away from the unstable equilibrium. The parameters of this noise are chosen to be close to experimentally relevant parameter ranges and noise structures, while remaining sufficiently close to the ground state. We then simulate the evolution of the system through the eGPE (unitary evolution) and implement a linear ramp of the scattering length into the supersolid regime to $a_s^f = 88a_0$, i.e., $a_s(t)/a_0 = 96 - 8t/\tau_Q$, with the ramp time set by τ_Q , which takes values between 1 ms and 770 ms. A schematic of the quench protocol is shown in Fig. 1(d). By including stochastic noise in the initial state, and performing

500 independent simulations with identical quench parameters, the dynamics are simulated within a truncated Wigner framework, thereby going beyond a pure mean-field analysis [79].

The variational parameters are fixed at $\ell = 1.08 \mu\text{m}$, $\eta = 4.25$, corresponding to the values in the ground state at $88a_0$. The total system size is selected to be approximately $L = 344 \mu\text{m}$ such that the ground state achievable by perfect adiabaticity would consist of exactly $N_{\text{uc}} = 128$ primitive unit cells of the supersolid crystal. See also the appendixes for results with zero temperature (quantum) noise only (Appendix A), and at larger system sizes (Appendix C).

For the fixed values of the variational parameters above, the critical point of the system is located at $a_c \approx 91.05a_0$. It should be noted that this is slightly shifted from the ground-state critical point $a_c^{(\text{GS})} \approx 90.5a_0$ [see previous section, Fig. 1(b), and Ref. [15]]. This shift is expected since ℓ and η vary slightly across the phase diagram and do not remain fixed. We do not expect this effect to have a significant impact on our results due to the continuous character of the transition. The shift of the critical point due to fixing the variational parameters is less than the shift set by using the dimensionally reduced theory. In Appendix B, we show some comparisons of our results with full 3D simulations.

Figure 2 shows a sample quench across the superfluid-supersolid transition for $\tau_Q = 100$ ms. In Fig. 2(a), a portion of the 1D density as a function of time is shown. Density modulations emerge after the critical point is crossed with an apparent delay compared with the expectation for an adiabatic crossing of the transition [80,81]. The nonuniformity of the density modulation front suggests that independent regions begin to form domains at different times. This is further emphasized in Fig. 2(b), which shows the full 1D density profile with clearly identifiable regions where the modulation has developed only locally. Figure 2(c) shows the number of density peaks as a function of time (averaged over 500 independent runs) relative to the expected number in the ground state (128 in this case), showing a smooth development of modulations after the transition is crossed. Furthermore, the quench appears to produce an excess of density modulation peaks, first overshooting the long-time average, and then settling to a value above unity within the time scales we consider here. The number of peaks does not settle down to the expected $N_{\text{peaks}} = N_{\text{uc}}$ within at least a hundred milliseconds, indicating that some frustration remains after the quench has been completed, and thus some excess energy remains. Such frustration has also been observed in phase transitions of other superfluids where coarsening dynamics does not occur in low-dimensional configurations [44,82].

III. SCALING PROPERTIES

A. Freeze-out time

According to KZM theory, for a linear quench across a continuous phase transition, the freeze-out time is known to scale as $\hat{\tau} \propto \tau_Q^{\zeta_{\text{KZ}}}$, where $\zeta_{\text{KZ}} = z\nu/(1+z\nu)$ as in Eq. (1). In our system, this indicates that there will exist a quench rate-dependent delay between the crossing of the phase transition and formation of a density modulated superfluid, indicative of a supersolid state.

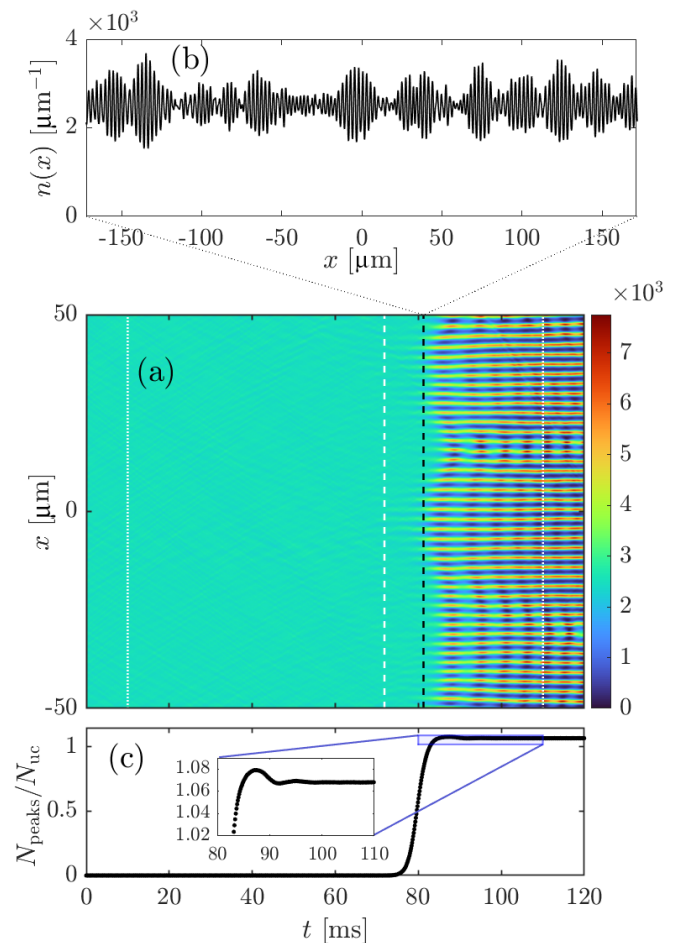


FIG. 2. Quench across the superfluid-supersolid transition. Panel (a) shows the density $n(z)$ of a part of the system, for a sample quench, equilibrating for 10 ms (leftmost dotted line), then ramping across the critical point (white dashed line) for 100 ms until the final value of $88a_0$ (right dotted line) is reached. A density cut along the black dashed line is shown in panel (b) for the full system. Panel (c) shows the number of supersolid peaks per ground-state unit cell as a function of time for the same quench rate as in panels (a) and (b), averaged over 500 independent noise realizations, with an inset showing an overshoot and rebound following the transition.

We characterize the emergence of the density modulation through the evolution of the superfluid fraction, estimated via Eq. (6) and ensemble averaged over 500 realizations. In Fig. 3, we show the dynamics of f^s , which we take to be an order parameter for the superfluid-supersolid transition. In Fig. 3(a), we plot f^s across the quench, shifted by the time at which the transition is crossed, $a_s(t_c) = a_c$, so that all quenches cross the transition at $t - t_c = 0$. After a delay, density modulation develops in the system, leading to a depression of the superfluid fraction. This reduction is nonmonotonic, and there are oscillations in f^s as the system exhibits a rebounding of the spatial density modulations. This oscillation suggests that an amplitude mode is excited, an example of which is the gapped Higgs excitation that emerges from the roton instability; see Sec. III D and Ref. [75] for a more in-depth discussion of the emergence of this Higgs mode. In all quenches, there is a final trend towards the ground-state superfluid fraction of

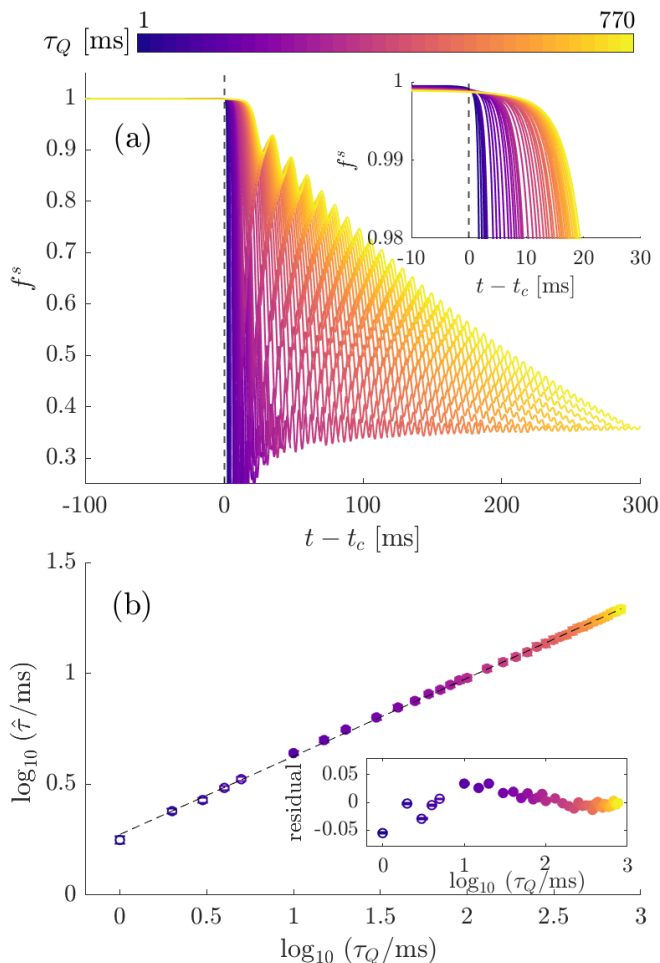


FIG. 3. Delay in supersolid formation for various quenches shown via the decrease of f^s from unity. Panel (a) shows the full evolution, with the inset focusing on the initial one-dimensional supersolid formation. Slower quenches lead to a greater delay in the formation of a supersolid following the crossing of the critical point. In panel (b), the time delay $\hat{\tau}$ at which the superfluid fraction drops below 0.98 is shown as a function of the quench time τ_Q , with the best fit $\hat{\tau} \propto \tau_Q^{0.352(3)}$ shown as a dashed straight line. Standard errors on the data are shown due to the statistical spread over 500 trials. The inset shows the normalized residuals from the data to the best fit. Open markers represent quenches past $88a_0$ (see main text).

approximately $f^s = 0.323$, settling slightly above this value with some oscillations remaining, indicating some residual excitations [see also discussion of Fig. 2(c)].

In order to avoid the influence of the excited amplitude mode and any coarsening effects it may have on the system, in this section we consider only the onset of supersolid formation by taking $\hat{\tau}$ to be defined by the difference between the time at which the critical point is crossed to when f^s first drops below 0.98, see inset to panel (a). Using this definition of $\hat{\tau}$, in Fig. 3(b), we show the scaling as a function of the quench time τ_Q . We see clear power-law scaling in agreement with Eq. (1) and fit $\hat{\tau} \propto \tau_Q^{0.352(3)}$. For the data in this and subsequent figures, we also plot the normalized residual, for Fig. 3 defined by $(\hat{\tau} - \text{fit}[\hat{\tau}])/\text{fit}[\hat{\tau}]$, where $\text{fit}[\hat{\tau}](\tau_Q) = A\tau_Q^{\zeta_{\text{KZ}}}$ is the best fit of $\hat{\tau}(\tau_Q)$ in terms of a pure power law, parametrized by a

real constant A and an exponent ζ_{KZ} . In Appendix E, we also demonstrate that the extracted ζ_{KZ} exponent can be used to rescale $f^s(t)$ at early times onto a single universal scaling function.

We select a broad range of quench times to cover what might be considered “reasonable” within an experimental setting, however it should be noted that, for inverse rates faster than roughly $\tau_Q \approx 10$ ms, the quench must be extended past the selected final $a_s = 88a_0$, and eventually into the insulating droplet phase (for all these points we choose a final $a_s = 60a_0$). This is because for very fast quenches, the finite width of the supersolid region would require stopping the ramp during the freeze-out time, resulting in an effectively nonlinear ramp. The quench protocol shown in the schematic of Fig. 1(d) becomes modified to follow the dashed line instead—starting and stopping at higher and lower values of the scattering length, respectively. Our measures of KZM should not depend on this fact, since we only concern ourselves with initial supersolid formation following the crossing of the critical point. However, it is important to note that from a practical point of view, there is, generically, an upper limit to how fast one can quench into a supersolid. Throughout the present work, we mark the data obtained by quenches that are taken past the supersolid phase boundary by open symbols.

B. Correlation length

During a linear quench, the correlation length remains frozen at a value $\hat{\xi}$ when entering the freeze-out regime, which, according to KZM theory, scales as $\hat{\xi} \propto \tau_Q^{\nu_{\text{KZ}}}$, with $\nu_{\text{KZ}} = \nu/(1 + z\nu)$, cf. Eq. (1). Typically, the one-body density matrix $g^{(1)}(x, x') = \langle \psi^*(x)\psi(x') \rangle$ is used to characterize the superfluid nature of condensates [6,83] (i.e., off-diagonal long-range order) and can be used to define a correlation length associated with the typical range of phase coherence. Since the transition to a supersolid is signaled by a growth of periodic diagonal long-range order via density modulations in a system that remains largely phase coherent on both sides of the transition, it can be characterized by the density-density correlation function, viz.,

$$g^{(2)}(x - x') = \frac{1}{\bar{n}^2} \langle \psi^*(x')\psi^*(x)\psi(x)\psi(x') \rangle, \quad (7)$$

where we take $\langle \dots \rangle$ to indicate an ensemble average, in this case corresponding to a statistical numerical average over 500 independent realizations of the initial noise. Translation invariance allows us to interpret the ensemble average also as a spatial average and so this function is evaluated directly in Fourier space via $g^{(2)}(x) = \mathcal{F}^{-1}[n(-k)n(k)](x)$. In Figs. 4(a)–4(c), the solid colored lines show this function for three sample quench rates at the onset of supersolid formation [i.e., when the superfluid fraction is crossing $f^s(t) = 0.98$].

Due to the periodic crystalline structure, $g^{(2)}$ is highly oscillatory while also decaying towards the background superfluid level at that instant. The decay of the initial oscillations indicates that there exists a range over which the supersolid has formed a regular density structure. We find that the numerically extracted $g^{(2)}$ is empirically well approximated by the function

$$\text{fit}[g^{(2)}](x) = \mathcal{A} + (1 - \mathcal{A}) \cos(\mathcal{K}x)e^{-x^2/\mathcal{X}^2}, \quad (8)$$

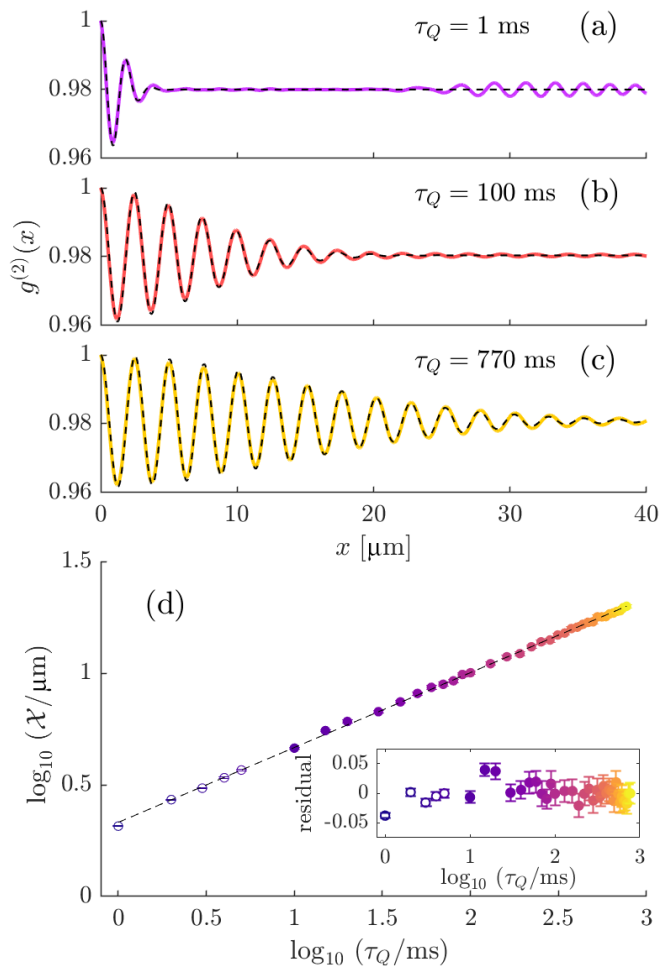


FIG. 4. Scaling of the correlation length. Panels (a)–(c) show the correlation function $g^{(2)}(x)$ (solid) for $\tau_Q = \{1, 100, 770\}$ ms, respectively. In each panel, $g_{\text{fit}}^{(2)}(x)$ is plotted as a black dashed line. Panel (d) shows the width \mathcal{X} for the fit $g_{\text{fit}}^{(2)}(x)$ for all quench durations. The best fit $\mathcal{X} \sim \tau_Q^{0.335(3)}$ is shown as a dashed straight line. Colors and marker filling match Fig. 3. The inset shows the normalized residuals $(\mathcal{X} - \text{fit}[\mathcal{X}])/\text{fit}[\mathcal{X}]$ of the best power-law fit $\text{fit}[\mathcal{X}] (\tau_Q) = B\tau_Q^{\nu_{\text{KZ}}}$ of \mathcal{X} .

where $\{\mathcal{A}, \mathcal{K}, \mathcal{X}\}$ are fitting parameters. In general, we expect \mathcal{A} to match closely with the average background superfluid value $f^s(t)$, while the wave vector \mathcal{K} of the modulation in $g^{(2)}$ captures the wave vector of the state's density modulation and should be close to the roton wave number k_{rot} that triggers the instability. The decay of supersolid correlations is set by the width \mathcal{X} , which we expect to scale as the correlation length.

In Figs. 4(a)–4(c), the best fit of the function $g^{(2)}(x)$ is shown as a black dashed line in each panel. Figure 4(d) shows the fit parameter \mathcal{X} over all quenches: we are able to observe a clear power-law scaling in agreement with Eq. (1), and plot $\log_{10}(\mathcal{X}/\mu\text{m})$ together with the corresponding KZM power-law fit, $\mathcal{X} \sim \hat{\xi} \sim \tau_Q^{0.335(3)}$. Similar scaling can be extracted by simply considering the width of a root-mean-squared envelope of $g^{(2)}(x)$ as the oscillations decay (not shown here). The decaying envelope indicates that regular periodic order is not maintained globally across the crystal, but rather that

the system forms locally regular domains that are globally incommensurate. There also appears to be a small revival in supersolid coherence in Fig. 4(a) that is not captured by our fitting function. We expect that revivals of this kind become less relevant with larger statistical ensembles. As in the case of the superfluid fraction, we are able to use the extracted ν_{KZ} in order to rescale $g^{(2)}(x)$ at different quench rates onto a universal scaling function, shown in Appendix E. In this case, it is only the envelope of the oscillations that scales universally, since the typical supersolid oscillation period is set by the roton.

The Gaussian spatial decay of the supersolid order is also notable, since generically order parameters will decay exponentially in the noncritical regime. Exceptions exist, for example, in free-fermion spin chains, where interdefect correlators follow Gaussian decay [84–87] following a quench. Nonconservative fields undergoing phase ordering (e.g., in the 1D XY model) at late times [88], beyond the Kibble-Zurek regime, can also yield transient Gaussian correlators.

C. Crystal phase and defect densities

Another way to define supersolid correlation is to identify a spatially varying crystal phase along the full system and evaluate the phase coherence over space. This definition is instructive and allows us to directly identify the defects in the crystal structure through phase jumps. Below, we describe how to define the crystal phase, check the scaling of the correlation length through that of the crystal phase coherence, and study the scaling of the number of defects.

The local phase ϕ of the crystal at a point $x = x_j$ can be defined in the following way:

$$\phi(x_j) = \frac{2\pi}{\bar{d}}(x_j - j\bar{d}), \quad (9)$$

where $\bar{d} = N_{\text{peaks}}^{-1} \sum_j (x_{j+1} - x_j)$ is the average peak-to-peak distance, and the prime indicates that the sum is taken over the density peaks, numbered from $j = 1$ to N_{peaks} . This phase is schematically depicted in Fig. 5(a), defining $\phi(x_j)$ as the normalized distance of the individual peaks from their respective adjacent minimum in some reference lattice with lattice constant \bar{d} (vertical dashed lines). In analogy with a perfectly coherent uniform superfluid, a globally coherent crystal would therefore have $\phi(x_j) = \text{constant}$. Numerically, this phase is the phase factor of a Fourier transform of each unit cell of size \bar{d} .

The supersolid coherence can also be quantified via its corresponding crystal phasor $e^{i\phi(x)}$ and its two-point correlation function,

$$C(x - x') = \langle e^{-i\phi(x)} e^{i\phi(x')} \rangle. \quad (10)$$

Unlike for $g^{(2)}$, the phase $\phi(x)$ is, in each run, only evaluated at the (randomly located) positions x_j of the density maxima, which results in a much coarser structure. Figure 5(b) shows the crystal correlation function (10) following the quench, at the moment t when the superfluid fraction drops below $f^s(t) = 0.98$, i.e., at $t = \hat{t}$. The full width at half maximum of $C(x)$ is proportional to the correlation length $\hat{\xi}$ at the freeze-out time and is then plotted as a function of quench time in

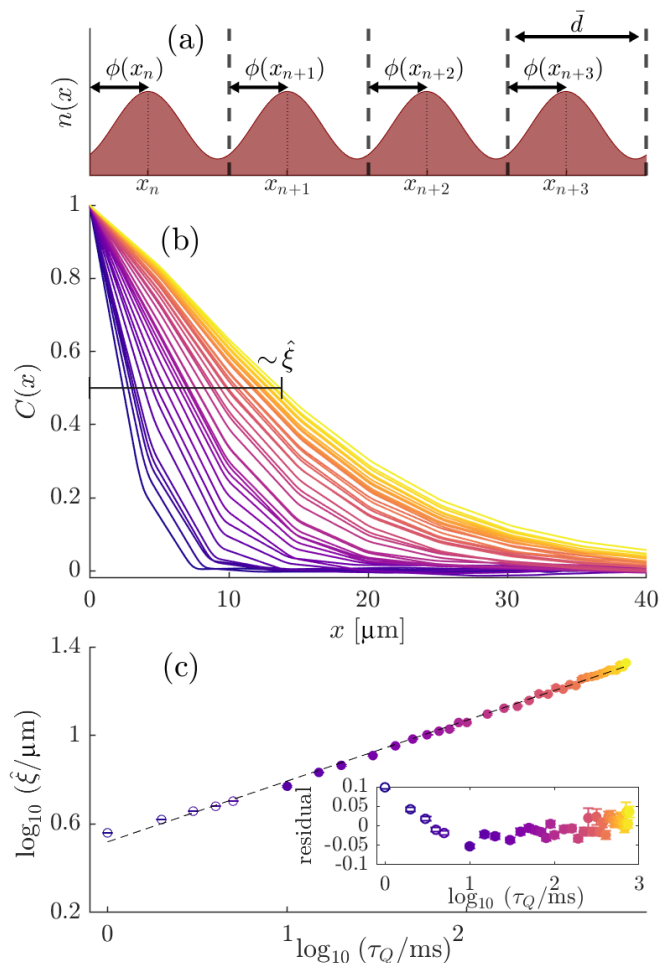


FIG. 5. Crystal phase and correlation function $C(x)$. A schematic for the crystal phase is shown in panel (a), where a modulated supersolid density structure with (in general unevenly spaced) peaks at x_j , marked with dotted lines. The normalized distance from those peaks to some reference set of points equally spaced by \bar{d} , shown as vertical dashed lines, gives the crystal phase $\phi(x_j)$ at that peak. Panel (b) shows the correlation function (10) for the same quenches as used for Fig. 3. The half width at half maximum is depicted in panel (c), together with the power-law fit $\hat{\xi} \propto \tau_Q^{0.275(3)}$, with the normalized residuals computed in analogy to those in Fig. 3 and shown in the inset. Colors and marker filling for panels (b) and (c) match those in Fig. 3.

Fig. 5(c). The extracted correlation length shows power-law scaling, $\hat{\xi} \propto \tau_Q^{0.275(3)}$, a somewhat smaller estimate than the scaling of $g^{(2)}$. In Appendix D, we discuss the close relationship between $C(x)$ and $g^{(2)}(x)$.

In computing $C(x)$, it is the averaging over hundreds of trials that ultimately smooths out the data. From the resulting averages, one obtains a smooth function that nevertheless develops kinks where its slope changes suddenly due to the higher likelihood of finding a lattice site below that distance. Importantly, at faster quenches, the separation of scales begins to break down: the width of $C(x)$ becomes on the order of the density modulation periodicity $L_{uc} \approx 2.6 \mu\text{m}$. Without the separation of scales, the notion

of a KZM domain and a supersolid defect becomes poorly defined.¹

The KZM is often associated with the formation of topological defects [89,90], which in the case of uniform superfluids typically take the form of vortices or solitons [30,31,33,35,41,61,91], presenting themselves as jumps in the phase, ultimately separating regions of different gauge symmetry. KZM-induced supersolid defects in the one-dimensional system can be understood instead as sudden jumps in the *crystal* phase ϕ , noted $\Delta\phi$. Based on the fundamental predictions of KZM theory quoted above, the defect density can be estimated to scale as

$$n_d \sim \frac{\xi^d}{\xi^D} \sim \left(\frac{1}{\tau_Q}\right)^{\frac{(D-d)v}{1+2v}} \equiv \tau_Q^{(d-D)v_{\text{KZ}}}, \quad (11)$$

where d and D are the dimensionality of the defects and system, respectively. In the case of sudden kinks in the crystal phase alone, we therefore expect our results to correspond to $d = 0$ and $D = 1$, indicating that the defect density scaling should match that of $\hat{\xi}$.

In Fig. 6, we plot the number of defects ($\propto n_d$) as a function of quench rate. Due to the continuous nature of ϕ , there remains some ambiguity as to the required size of the crystal phase jump to correspond to a defect. We therefore show the scaling for a range of phase jumps corresponding to $\Delta\phi > \{\pi/6, \pi/5, \pi/4, \pi/3, 2\pi/5, \pi/2\}$. In all cases, a clear scaling of the number of defects with the quench rate is observed. At faster quench rates, the data appear to curve and saturate towards a behavior that indicates that the defect density begins to be independent of the quench rate. In our case, we again attribute this to the breakdown of scale separation in our system: typical KZM domain sizes begin to approach the crystal wavelength, below which any notion of a supersolid defect becomes poorly defined. This saturation behavior has also been seen in other systems [50,53,56] and has been described in terms of a universal breakdown [92] of the KZM at fast quench rates.

In order to select an appropriate definition of a crystal defect, we consider their number distribution statistics. In what has become known as beyond-KZM physics [93,94], universality in defect formation is not restricted to their mean number, but the distribution itself. Since defect formation due to the KZM corresponds to statistically independent events (random successes of Bernoulli trials at different points in space), the discrete probability distribution is binomial [95,96]. In the continuum limit, where the defects are sufficiently dilute to remain uncorrelated, we therefore expect the probability of counting \mathcal{N} defects to obey a Poisson distribution [93,97,98],

$$P(\mathcal{N}) = \frac{1}{\mathcal{N}!} \lambda^{\mathcal{N}} e^{-\lambda}, \quad (12)$$

where the expected value $\lambda = \langle \mathcal{N} \rangle$ is then set by the quench rate according to the standard KZM scaling.

¹We therefore suggest that care must be taken when using a function like $C(x)$ to determine KZM scaling results, especially at quench rates where ξ begins to approach L_{uc} , and perhaps greater statistics are needed for proper convergence of this measure.

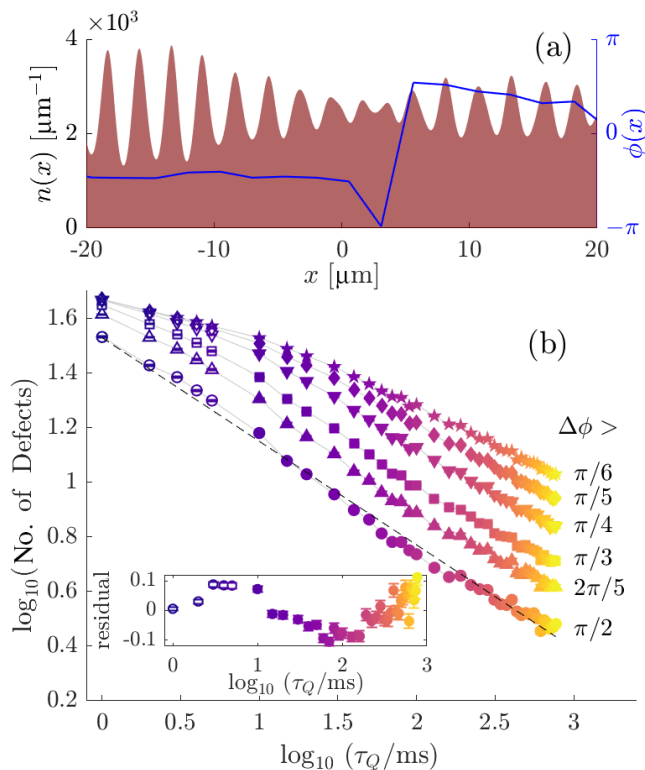


FIG. 6. Defect density scaling. Panel (a) illustrates a crystal defect from one simulation run in the density $n(x)$ (brown shaded area) and the crystal phase $\phi(x)$. Defects are identified as local jumps in the crystal phase $\phi(x)$. Panel (b) reports on the number of crystal defects observed at the supersolid formation time for different minimum thresholds of phase jumps, $\Delta\phi > \{\pi/6, \pi/5, \pi/4, \pi/3, 2\pi/5, \pi/2\}$, marked as {circles, triangles, squares, inverted triangles, diamonds, stars}, respectively. Light-gray lines along data sets with the same defect size are shown to guide the eye. The best fit line for $n_d \propto \tau_Q^{-\nu_{\text{KZ}}}$ is shown for $\Delta\phi > \pi/2$ only (dashed). Normalized residuals determined in analogy to those in Fig. 3 are shown in the inset. Colors and marker filling for panel (b) match those in Fig. 3.

For a selection of defect sizes and quench rates, we plot in Fig. 7 the defect count probabilities within our total system following a quench, and compare them to the best-fit Poisson distribution curves $P(\mathcal{N})$. The difference between the curves is quantified through the average sum of squared residuals (RSS). A stricter definition of a defect (i.e., larger $\Delta\phi$) leads to better agreement (smaller RSS) with Poisson distributions across different τ_Q , while smaller phase jumps yield narrow peaks that disagree with the Poissonian hypothesis, especially at fast quench rates. Deviations from Poisson statistics imply that the phase jumps being counted no longer result from independent random events and thus are no longer “defects” in the KZM sense, but are somehow correlated. We suspect that small changes in the crystal regularity may not only arise due to KZM scaling, but as excitations in the crystal due to propagation of, e.g., sound modes (phonons) within an otherwise coherent domain.

The analysis of Fig. 7 indicates that a strict definition of a defect, using a large minimal phase jump $\Delta\phi > \pi/2$ is required for identifying KZM defects. Returning to Fig. 6 we

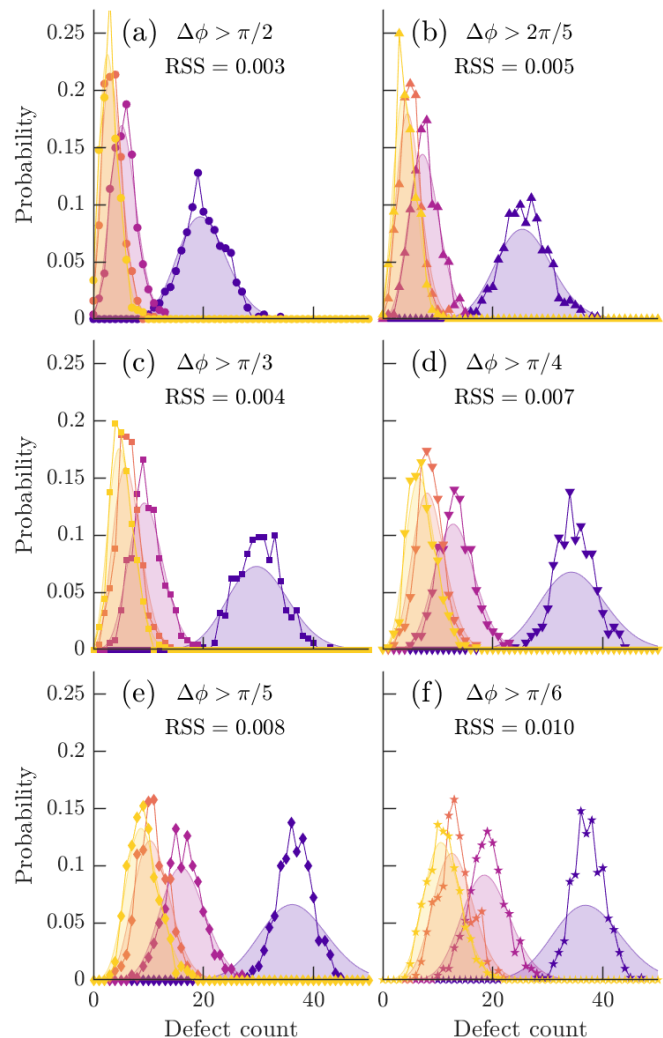


FIG. 7. Defect counting statistics. The probability of occurrence of a certain number of phase jumps within a fixed system size L is plotted (filled symbols) for different $\tau_Q \in \{10, 100, 404, 709\}$ ms, and different $\Delta\phi$ (see panel captions, symbols match those in Fig. 6). The Poisson distribution corresponding to the maximum likelihood estimate for λ for each dataset is shown as a shaded area. Lines serve as a guide to the eye. The residual sum of squares (RSS) is quoted in each panel. Colors match those in Fig. 3

fit the τ_Q scaling of the numbers of defects with $\Delta\phi > \pi/2$ with a power law and extract $\nu_{\text{KZ}} = \frac{\nu}{1+\nu} \approx 0.37(2)$. This scaling measure is independent of the $g^{(2)}$ scaling of the correlation length in Sec. III B and again appears to give a scaling result relatively close to $1/3$, albeit it is slightly outside the standard error bounds. We would also like to remark here that considering defects with large phase jumps may introduce a larger statistical spread: With the system sizes we simulate here, slow quench rates may only produce a handful of defects ($\lesssim 5$), and so the relative point spread error due to a single defect can be large. In the following section, we shall further examine the compatibility of these results with respect to critical scaling exponents as extracted from Bogoliubov theory.

We note that, in the above analysis, we did not consider the influence of extended ($d = 1$) excitations playing a role

in supersolid formation. It is known that, for the temperature-quench-induced BEC transition [50,57], the interplay between defects of different dimensions (e.g. vortices vs solitons) may hybridize the scaling result of Eq. (11). Similarly, any incidence of nonlinear excitations induced by the transition or by the initial thermal fluctuations would therefore, in principle, also contribute to the flattening of the curves in Fig. 6.

D. Scaling exponents

Using the numerical results for ζ_{KZ} and ν_{KZ} from Secs. III A and III B, respectively, we extract the scaling exponents,

$$\nu = 0.57(1), \quad (13)$$

$$z = 1.05(2), \quad (14)$$

for the superfluid-to-supersolid transition.

We may compare these dynamical KZM results to equilibrium estimates within the mean-field approximation. The characteristic time scale of a system near a quantum critical point is determined by the inverse of the energy gap, which closes as $\Delta \sim |\lambda - \lambda_c|^{z\nu}$ near the critical value λ_c of some tuning parameter λ [99]. Meanwhile, in the theory of dynamical critical phenomena [100] the low-energy vs low-momentum scaling of the dispersion defines the dynamical critical exponent as $\omega \propto k^z$. In the uniform superfluid, the dispersion relation can be calculated analytically within Bogoliubov theory based on the eGPE [73],

$$\hbar\omega = \sqrt{\frac{\hbar^2 k^2}{2m} \left(\frac{\hbar^2 k^2}{2m} + \frac{6\gamma_{\text{QF}}\hbar^{3/2}}{5\pi^{3/2}\ell^3} + \frac{gn}{\pi\ell^2} + 2n\tilde{U}^{\text{1D}}(k) \right)}, \quad (15)$$

while in the supersolid phase, only numerical solutions are possible. At zero temperature and for $a_s > a_c \approx 91.05a_0$, there exists a single gapless low-energy sound branch (i.e., Goldstone mode) associated with the phase rigidity of the system. At higher k , the attractive contribution of the DDI results in a rotonic minimum at momentum $k = k_{\text{rot}}$ and of energy ϵ_{rot} , and it is the softening and instability of the roton mode that leads to supersolid formation, see, e.g., Ref. [15]. Figure 8(a) shows the dispersion relation in the uniform regime (green curves), with a roton minimum developing as a_s is reduced. In the regime of the phase diagram where the transition is continuous, the onset of supersolidity occurs as the roton minimum touches zero, $\epsilon_{\text{rot}} = 0$ (black curve, $a_s = a_c$), and proceeds to go unstable.

The emergence of periodic density modulation in real space also leads to a periodic dispersion in momentum space and thus to a band structure. Figure 8(b) shows the band structure precisely at the critical point, with the Brillouin zone (BZ) edges set at multiples of the roton momentum at criticality, $k_{\text{rot}} \equiv k_c$, see, e.g., Ref. [75]. This corresponds to the mapping of the dispersion relation at $a_s = a_c$ of Fig. 8(a) into the first BZ. In this mapping, the roton minimum yields a second Goldstone (crystal-sound) mode associated with the breaking of the translational symmetry, and a third branch, which appears gapless at the transition. Precisely at the critical point, the roton wavelength sets the unit cell length via $L_{\text{uc}} = 2\pi/k_c$; however, the unit-cell size does not remain constant throughout the supersolid regime. Just below the transition,

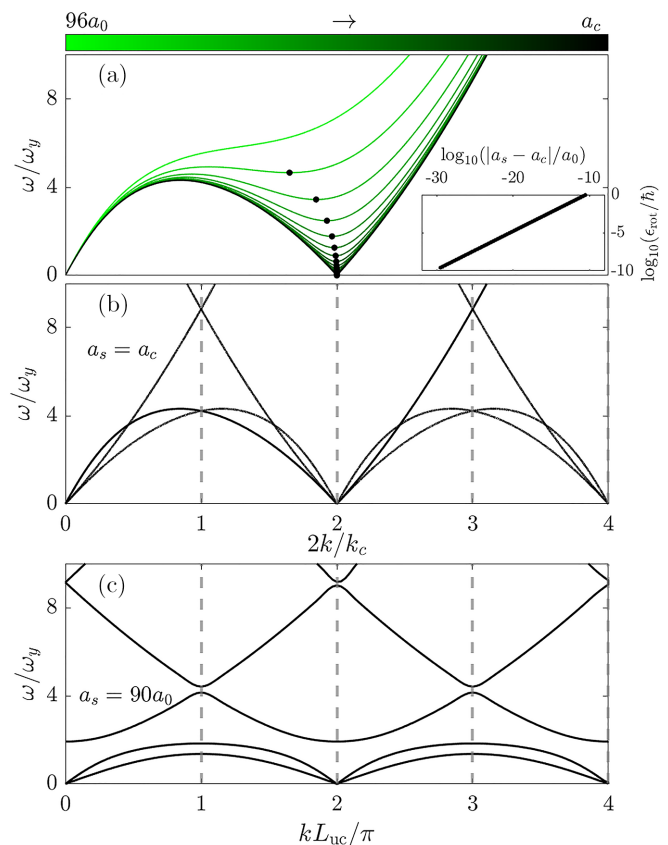


FIG. 8. Panel (a) shows the dispersion relation and the closing of the roton gap from Bogoliubov theory [Eq. (15)] as a_s is tuned through the superfluid regime. The roton minimum is marked by black circles. The scaling of the roton gap as a_s approaches $a_c \approx 91.05a_0$ from above is shown in the inset and satisfies $\epsilon_{\text{rot}} \sim \sqrt{a_s - a_c}$. Panel (b) shows the mapping of the spectrum at the critical point [black curve in panel (a)] into a periodic Brillouin-zone structure with periodicity $k_{\text{rot}} \equiv k_c$. Panel (c) shows the dispersion in the supersolid regime with a periodic Brillouin-zone structure whose periodicity is $2\pi/L_{\text{uc}}$. BZ edges are marked as vertical gray dashed lines. The excitation frequencies ω are shown in units of the transverse trapping frequency $\omega_y = \omega_z = 2\pi \times 150$ Hz.

as shown in Fig. 8(c) for $a_s = 90a_0$, the dispersion relation shows two gapless Goldstone modes while a gap (re)opens in the first branch at $k = \{0, k_c, 2k_c, \dots\}$, corresponding to the Higgs mode that drives the amplitude of density modulations.

Within Bogoliubov theory, we therefore expect the characteristic time to scale inversely to the closing of the rotonic energy gap [99],

$$\tau^{-1} \sim \epsilon_{\text{rot}} \sim |a_s - a_c|^{z\nu}. \quad (16)$$

It has been previously shown [73] and is verified here in the inset to Fig. 8(a) that the roton gap closes as $\epsilon_{\text{rot}} \sim \sqrt{a_s - a_c}$ so that $z\nu = 1/2$. Meanwhile, precisely at the critical point, the dispersion relation linearizes around the roton momentum,

$$\epsilon_{\text{rot}} \propto |k - k_c|, \quad (17)$$

and from the BZ mapping, the gapless roton mode emerges periodically about the zone edges, $\epsilon_{\text{rot}} \propto |k - mk_c|$, $m \in \mathbb{Z}$. Due to the linearization of the dispersion relation around mk_c , for the superfluid to one-dimensional supersolid transition

considered here, Bogoliubov theory suggests $z = 1$. Interestingly, while the presence of the Lee-Huang-Yang (LHY) correction to Eq. (5) and by extension Eq. (15) does change the location of the critical point slightly, it does not change the exponents extracted using Bogoliubov theory [73]. In this sense, the analytic “mean-field” analysis is not changed by the inclusion of a beyond-mean-field correction. A direct numerical analysis without the LHY correction is not possible, since the supersolid state requires stabilization.

The scaling exponents extracted from our numerical simulations, $\nu = 0.57(1)$ and $z = 1.05(2)$, appear compatible with the mean-field scaling exponent extracted from Bogoliubov theory, $\nu = 1/2$, of the correlation length and the quantum-critical value $z = 1$ of the dynamical exponent, although these fall slightly outside the statistical error bars of our results. Our numerical simulations go beyond mean-field dynamics, not because of the inclusion of the LHY correction, but because they are performed with a truncated Wigner framework [79,101,102], which incorporates classical fluctuations in a fully nonperturbative manner. The close agreement between the extracted exponents and mean-field theory may be due to the scaling behavior being relatively independent from beyond-mean-field effects, e.g., as in the case of systems above the upper critical dimension. Due to the relatively low depletion (typically less than 5% in our simulations at 20 nK here), we can expect modifications arising from interaction with excitations to be negligible.

A universality class that we had foreseen to apply to our transition is that of the $(D + 1)$ -dimensional XY model, with $D_{lc} = 1$ and $D_{uc} = 3$ being the respective lower and upper critical dimensions. In our case, $D = 1$, such that the transition would be of the Berezinskii-Kosterlitz-Thouless (BKT) type [103–106], for which a nonpolynomial correlation length and relaxation time scaling could be expected, which reaches power-law scaling with $\nu \rightarrow \infty$, $z = 1$ only asymptotically, for exponentially large quench times τ_Q [104]. This is in contrast to the clean power-law scaling observed here already for relatively small τ_Q , resulting in the above near-mean-field value of the exponent ν . Furthermore, Blakie *et al.* [75], who examined the critical behavior at the continuous superfluid-supersolid transition line, using Bogoliubov theory, found that there is a discontinuity in the compressibility, consistent with the transition being second order (the single exception being at the tip of the phase transition curve, which we do not encounter in any quenches performed in this paper). This discontinuity contrasts with the BKT expectation and supports the hypothesis of a universality class different from $(1 + 1)$ DXY. Even in $D = 3$ spatial dimensions, i.e., at the upper critical dimension of the XY model, the exponents, near the quantum critical point, would receive small anomalous contributions, and $z \simeq (D + 1)/2 = 2$ instead of the exponent $z \simeq 1$ we find, which is indeed compatible with dynamical critical scaling in $D = 1$ dimensions [100]. The exact universality class of the transition remains undetermined. We, however, note that our extracted near-mean-field exponents have been previously found to characterize the universality class for the superfluid-to-Mott insulator transition in the Bose-Hubbard model in $D \geq 3$ spatial dimensions, when crossing precisely at the Mott lobe tips with integer filling factor, i.e., at the quantum multicritical point [107,108], and exponents similar to our

KZM results have been previously observed in density-wave order (supersolid) transitions in $D = 2$ dimensions [109].

IV. CONCLUSION

We have explored the formation of a supersolid in an elongated dipolar quantum gas following a quench of the scattering length, using a reduced 3D model and via the extended Gross-Pitaevskii equation. We extract power-law scaling exponents corresponding to diverging relaxation time and correlation length scales. In particular, the divergence in relaxation time was estimated by identifying the freeze-out time with the delay in supersolid formation during the quench. The supersolid correlation length scaling was extracted by fitting a spatially oscillating function with a Gaussian-shaped envelope to the density-density correlation function $g^{(2)}(x)$. We found that the results for the extracted critical exponents $\nu = 0.57(1)$ and $z = 1.05(2)$ appear to be nearly compatible with the corresponding values expected from mean-field theory. When considering a measure for the crystal phase $\phi(x)$, we found that there appears to be a systematic breakdown of scaling results and an onset of defect density saturation at very fast quench rates. We posit that this breakdown [92] is explained by the fact that typical KZM domain sizes in the supersolid approach the crystal lattice size set by the roton. Nevertheless, over multiple orders of magnitude, defect densities appear to obey power-law scaling.

We consider an elongated system for statistical purposes; however, our study is performed with experimental considerations in mind. In particular, we selected parameters corresponding to ^{164}Dy , including scattering lengths, typical trap frequencies, and reasonable temperatures used in dipolar quantum gas experiments [9–11]. For a dipolar gas confined in a harmonic trap, the direct applicability of our results will depend on the cloud aspect ratio and quench rates [41], since in some regimes the inhomogeneous KZM [33,57] may lead to a different set of exponents. One candidate for the uniform tubular geometry we have proposed is a ring-shaped trap [110–112], which has been realized for ^{23}Na [113–116] and ^{87}Rb [47,117–122], and has been theoretically shown to support the dipolar supersolid phase [123,124]. While supersolid lifetimes remain a challenge for these experiments, particularly due to high densities in the dipolar droplets, the advantage of the measures we have introduced in this paper is that only the onset of supersolidity needs to be considered; thus, long lifetimes are not required to verify our results.

An interesting future direction is to consider melting the supersolid via a reverse-quench protocol [86,125–127], allowing us to probe the symmetrical of the KZM schematic curves shown in Fig. 1. Finally, we have only focused on the transition from the uniform superfluid to a one-dimensional droplet chain. If an additional trapping direction is relaxed, there exist transitions to many more kinds of two-dimensional supersolid lattices that are also possible, leaving the door open to further examination of dynamical symmetry breaking in more complex supersolids.

ACKNOWLEDGMENTS

The authors thank M. Ballu, R. Bisset, T. Bland, K. Chandrashekar, J. Gao, C. Götzhäuser, P. Heinen, L. Hoenen,

G. Lamporesi, A. Oros, E. Poli, G.-X. Su, and N. Rasch for helpful discussions and collaboration on related work. They acknowledge support by the Deutsche Forschungsgemeinschaft (DFG, German Research Foundation), through SFB 1225 ISOQUANT (Project-ID 273811115), Grant No. GA677/10-1, and under Germany's Excellence Strategy – EXC 2181/1 – 390900948 (the Heidelberg STRUCTURES Excellence Cluster), and by the state of Baden-Württemberg through bwHPC and the DFG through Grants No. INST 35/1134-1 FUGG, No. INST 35/1503-1 FUGG, No. INST 35/1597-1 FUGG, and No. 40/575-1 FUGG (MLS-WISO, Helix, and JUSTUS2 clusters). W.K. acknowledges the support of the Natural Sciences and Engineering Research Council of Canada (NSERC) [funding Reference No. PDF-577924-2023]. L.C. acknowledges support by the European Research Council (ERC) under the European Union's Horizon Europe research and innovation program under Grant No. 101040688 (project 2DDip).

Views and opinions expressed are those of the authors only and do not necessarily reflect those of the European Union or the European Research Council. Neither the European Union nor the granting authority can be held responsible for them.

APPENDIX A: THERMAL AND QUANTUM NOISE

In the variational 1D simulations, thermal and quantum noise are included via

$$\psi(x, 0) = \sqrt{\bar{n}} + \sum_l' [A_l^+ e^{ik_l x} + A_l^- e^{-ik_l x}], \quad (\text{A1})$$

where A_l^\pm are Gaussian random variables subject to $\langle |A_l^+|^2 \rangle = \langle |A_l^-|^2 \rangle = (e^{\epsilon_l^f/k_B T} - 1)^{-1} + \frac{1}{2}$ for temperature T and free-particle dispersion $\epsilon_l^f = 2\hbar^2 l^2 / (mL^2)$ for $l \in \mathbb{N}^+$. The sum \sum_l' is restricted to eigenstates such that $\epsilon_l^f < 2k_B T$.

In full 3D calculations (see Appendix B), thermal and quantum noise include amplitudes in the transverse harmonic oscillator modes,

$$\Psi(\mathbf{r}, 0) = \sqrt{\bar{n}} + \sum_{l\gamma\delta}' \phi_\gamma(y) \phi_\delta(z) [A_{l\gamma\delta}^+ e^{ik_l x} + A_{l\gamma\delta}^- e^{-ik_l x}], \quad (\text{A2})$$

where now $\langle |A_{l\gamma\delta}^+|^2 \rangle = \langle |A_{l\gamma\delta}^-|^2 \rangle = (e^{\epsilon_{l\gamma\delta}/k_B T} - 1)^{-1} + \frac{1}{2}$ for dispersion $\epsilon_{l\gamma\delta} = \hbar\omega_\gamma(\gamma - \frac{1}{2}) + \hbar\omega_\delta(\delta - \frac{1}{2}) + 2\hbar^2 l^2 / (mL^2)$, now with $l, \gamma, \delta \in \mathbb{N}^+$. The sum has again been restricted such that $\epsilon_{l\gamma\delta} < 2k_B T$.

In the main text, we consider a system populated with stochastic noise drawn from a thermal distribution at 20 nK. We have assumed that this is close enough to zero temperature such that we are not greatly affecting the location of the transition due to thermal effects. Here, we verify that this assumption holds by considering quenches where the only source of noise is a half-particle per mode. Specifically, we populate modes as in Eq. (A1), but A_l^\pm are now subject to the zero-temperature limit $\langle |A_l^+|^2 \rangle = \langle |A_l^-|^2 \rangle = 1/2$. Rather than a temperature-dependent cutoff, we now restrict the sum to include states with momenta less than the inverse healing length: $k^{-1} < \xi_h = \hbar/\sqrt{m\mu}$. In this limit, the particle and energy added due to noise have been reduced to less than 1%.

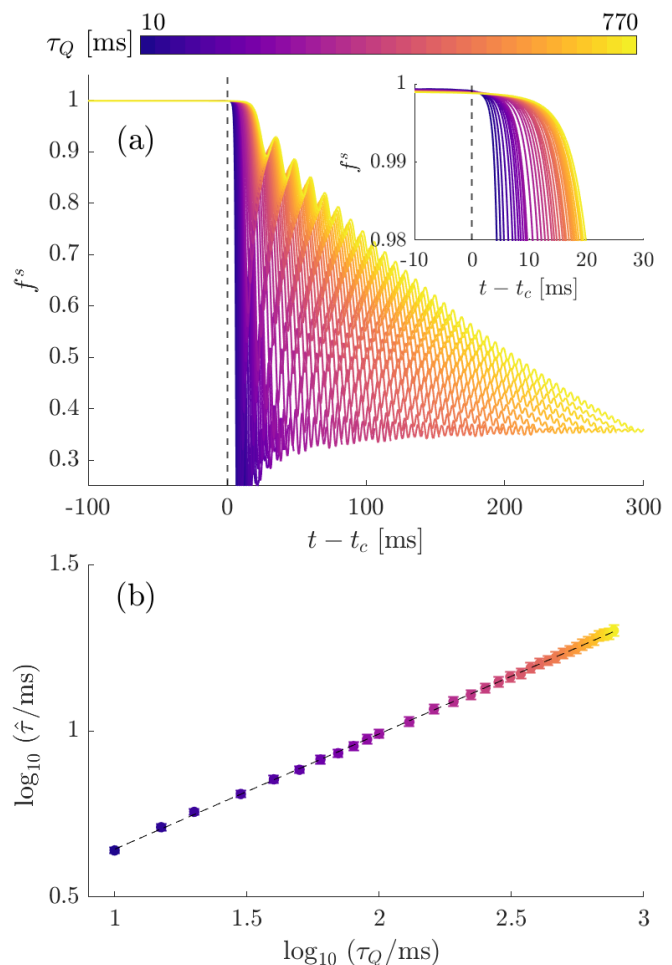


FIG. 9. Delay in supersolid formation, similar to Fig. 3, with the only difference being that each simulation is populated only with quantum noise. As in the main text, panel (a) shows the full $f^s(t)$ with an inset focusing on the initial moments after crossing the critical point. In panel (b), we show the time delay, with the best fit $\hat{\tau}_{T=0} \propto \tau_Q^{0.346(2)}$.

In Figs. 9 and 10, we present the results for our system populated only with the zero-temperature quantum noise described above, rather than the low-temperature thermal noise of the main text. In these figures, we have selected again the same system size as described in the main text, now averaged over 400 independent trials. The resulting scaling, described in the captions of each figure, seems to indicate that there is very minimal difference due to the choice of noise. This indicates that the $T = 20$ nK noise used in the main text is sufficiently small for our parameters to be considered representative of dynamics to be expected in the zero-temperature limit.

APPENDIX B: COMPARISON WITH THREE-DIMENSIONAL SIMULATIONS

Here, we compare our results with full 3D simulations, i.e., evolving under Eq. (2), for select quench rates. Similar to the variational model, we perform quenches from $a_s = 96a_0$ to $a_s = 88a_0$, now with a grid size of $\approx 160 \mu\text{m}$, corresponding to 64 unit cells in the supersolid ground

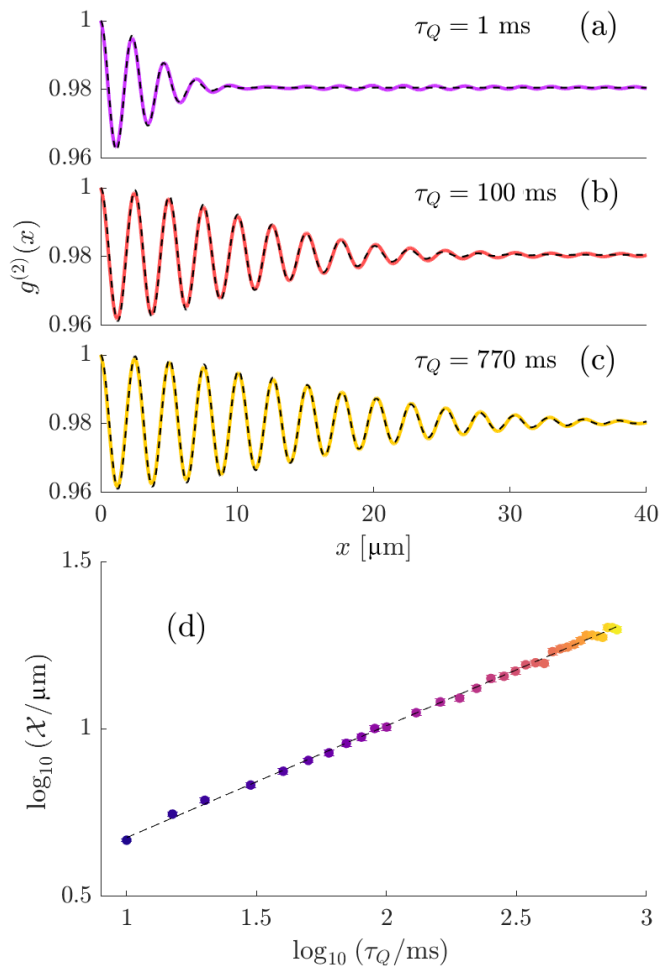


FIG. 10. Similar to Fig. 3 of the main text, now with quenches where the initial state is populated with quantum noise only. Panels (a)–(c) show the density-density correlation function at the indicated times, and panel (d) shows the envelope scaling as in the main text, with $\mathcal{X}_{\tau=0} \sim \xi \sim \tau_Q^{0.334(5)}$.

state at $88a_0$. At $\bar{n} = 2500 \mu\text{m}^{-1}$, 3D simulations indicate that the critical point is located at $a_s = a_c^{3D} = 92.27a_0$ [16]. Due to the size of the simulation grids and the resulting datasets, the results are averaged over only five realizations each of the noise in Appendix A, and for a more limited range of τ_Q , resulting in much larger standard errors in the data.

The superfluid fraction f^s as a function of time is presented in Fig. 11(a). Similar to the main text, we can extract the supersolid delay by the time it takes for f^s to drop below 0.98. The scaling of the delay is plotted in Fig. 11(b), along with the corresponding quench data using the variational model. We are able to extract $\hat{\tau}_{3D} \propto \tau_Q^{0.33(1)}$, which, within the error range quoted, is compatible with our results from the reduced model.

We can also measure the $g^{(2)}$ correlation function along the z axis for full 3D simulations, as shown in Fig. 12. Similar to Fig. 4 of the main text, we plot in Figs. 12(a)–12(c) the correlation function $g^{(2)}(x)$, now after integrating out the wavefunction in the radial directions, $\psi(x) = \int dydz\Psi(\mathbf{r})$, for $\tau_Q = \{10, 60, 161\}$, respectively. Figure 12(d) shows the

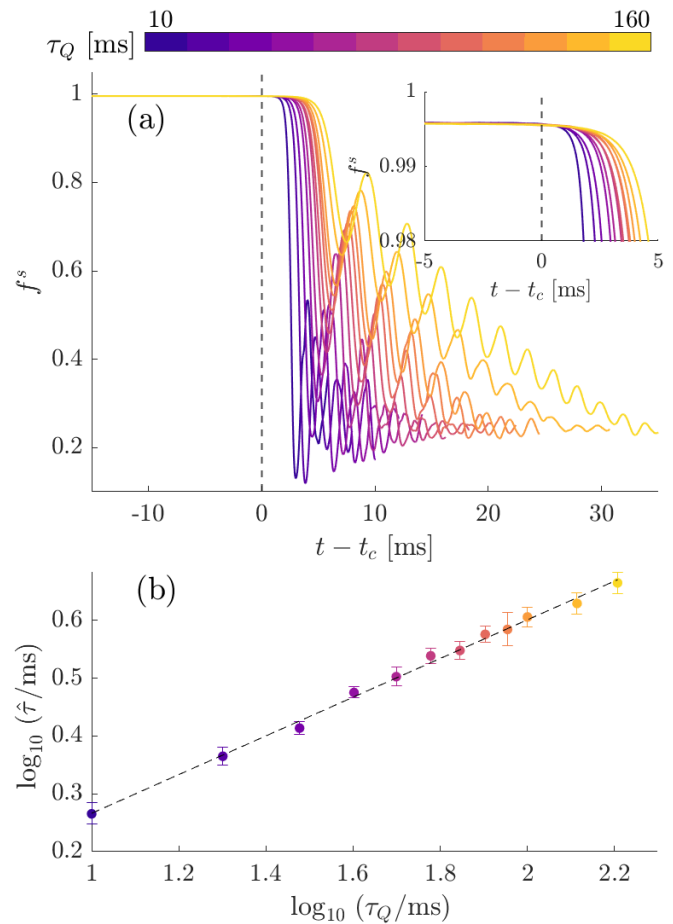


FIG. 11. Delay in supersolid formation for various quenches for full 3D simulations. Similar to Fig. 3 of the main text, panel (a) shows the full $f^s(t)$, with the inset focusing on the initial supersolid formation. Panel (b) shows the time delay at which f^s crosses 0.98, indicating supersolid formation, with the best fit $\hat{\tau}_{3D} \propto \tau_Q^{0.33(1)}$ shown as a dashed line. Note that the difference in colorbar scale from the other figures, which is due to the limited range of τ_Q .

best fit \mathcal{X} from Eq. (8), giving an approximate scaling of $\mathcal{X} \sim \hat{\xi} \sim \tau_Q^{0.40(16)}$.

APPENDIX C: SYSTEM LENGTH DEPENDENCE

In this appendix, we present results for the freeze-out time and correlation functions in our reduced theory for system sizes consisting of 1024 unit cells, compared to 128 in the main text. The aim of this section is to verify that finite-size effects do not strongly affect the main results of the paper. Due to the large size of the system, we only perform 10 quenches for each τ_Q .

Figure 13 shows the superfluid fraction over time in the longer system, governed by Eq. (5). The results for the freeze-out time appear to be similar to the results of the shorter system in the main text, with an extracted scaling of $\hat{\tau}_{\text{long}} \propto \tau_Q^{0.344(1)}$. This result is not unexpected: for a uniform system, the delay in supersolid formation should not depend on the system size. It is notable that relatively few trials are sufficient to give similar results to the main text.

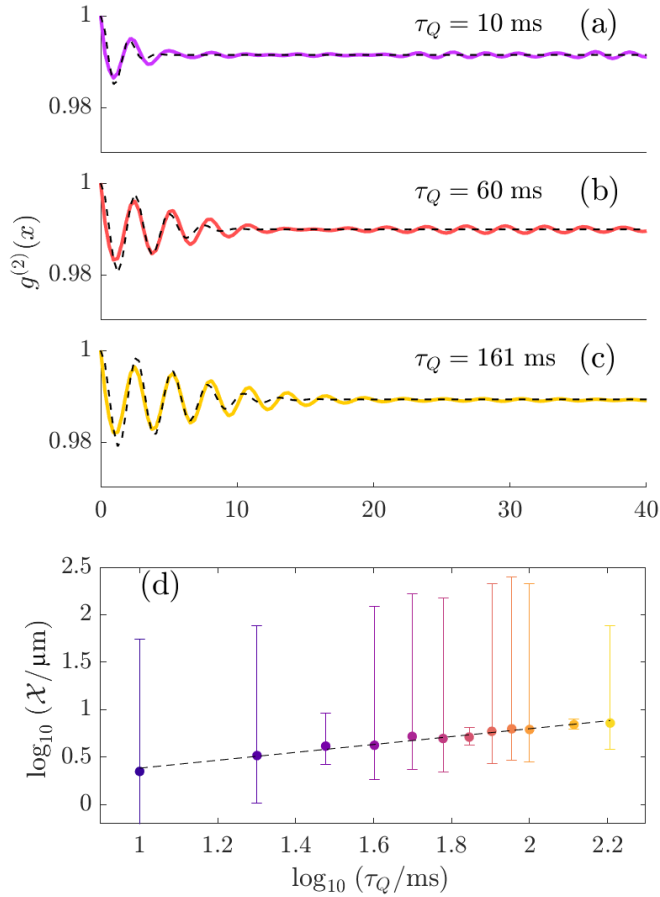


FIG. 12. Supersolid correlation length $g^{(2)}(x)$, similar to Fig. 4, now for 3D simulations, at $\tau_Q = \{10, 60, 161\}$ in panels (a)–(c), respectively, giving an approximate scaling of $\mathcal{X}_{3D} \sim \hat{\xi} \sim \tau_Q^{0.40(16)}$.

In Fig. 14, we show the correlation function $g^{(2)}(x)$ similarly to Fig. 4 of the main text, now for the longer system. We again perform a fit according to Eq. (8) at the onset of supersolid formation, and extract a scaling result of $\mathcal{X} \sim \hat{\xi} \sim \tau_Q^{0.332(8)}$, similar to the main text. Due to the fact that $g^{(2)}(x)$ is spatially averaged over a much longer system, the results presented here do not suffer from any dramatic loss of statistics due to averaging over only 10 quenches. However, the limited number of quenches does prevent us from achieving statistically meaningful results in terms of defect counting, so we do not attempt any analysis of defect density scaling in the longer system.

APPENDIX D: RELATIONSHIP BETWEEN $g^{(2)}$ AND $C(x)$

Assuming the following ansatz for the density:

$$n(x) = \bar{n} + \lambda \cos[kx + \phi(x)], \quad (D1)$$

where $\phi(x)$ is some locally varying phase, and λ is the strength of the supersolid modulation, the correlation function can be

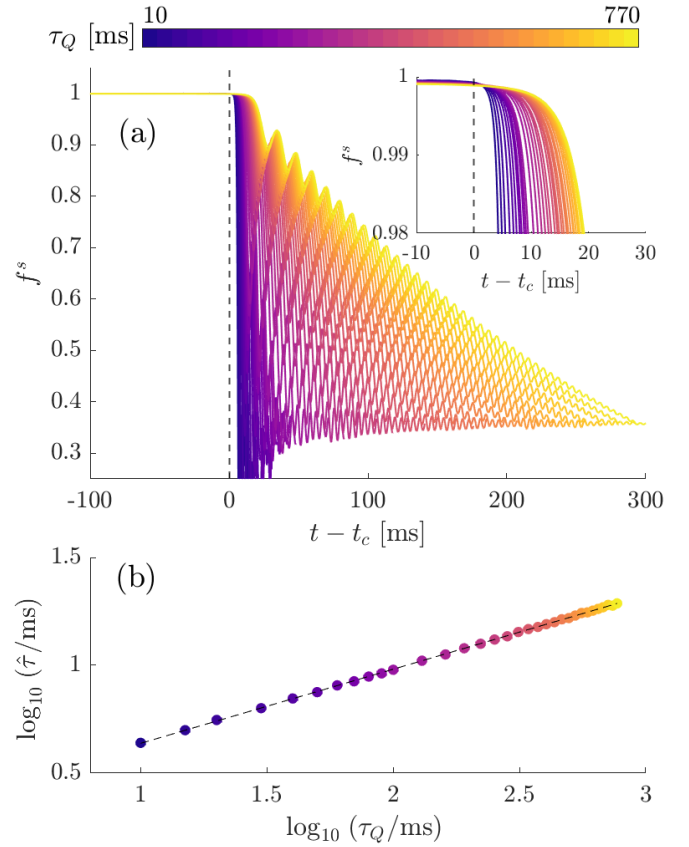


FIG. 13. Delay in supersolid formation in the reduced theory for a much longer system size of 1024 unit cells. Similar to Fig. 3 of the main text, panel (a) shows the full $f^s(t)$, along with a zoomed-in inset. Panel (b) gives the log-log time delay at which f^s crosses 0.98, with the best fit as a dashed line.

determined from

$$\begin{aligned} n(x)n(x') &= \{\bar{n} + \lambda \cos[kx + \phi(x)]\} \\ &\times \{\bar{n} + \lambda \cos[kx' + \phi(x')]\} \\ &= \bar{n}^2 + \bar{n}\lambda \{\cos[kx + \phi(x)] + \cos[kx' + \phi(x')]\} \\ &\quad + \lambda^2 \cos[kx + \phi(x)] \cos[kx' + \phi(x')] \\ &= \bar{n}^2 + \bar{n}\lambda \{\cos[kx + \phi(x)] + \cos[kx' + \phi(x')]\} \\ &\quad + \frac{\lambda^2}{4} [e^{i(kx + \phi(x))} + e^{-i(kx + \phi(x))}] \\ &\quad \times [e^{i(kx' + \phi(x'))} + e^{-i(kx' + \phi(x'))}]. \end{aligned} \quad (D2)$$

Averaged over realizations, terms like $\cos[kx + \phi(x)]$ will vanish, leaving

$$\begin{aligned} \langle n(x)n(x') \rangle &= \bar{n}^2 + \frac{\lambda^2}{4} (e^{i(k(x+x') + \phi(x) + \phi(x'))} \\ &\quad + e^{i(k(x-x') + \phi(x) - \phi(x'))} + \text{H.c.}) \\ &= \bar{n}^2 + \frac{\lambda^2}{4} (e^{2ikR} e^{i(\phi(x) + \phi(x'))} \\ &\quad + e^{i(ks + \phi(x) - \phi(x'))} + \text{H.c.}), \end{aligned} \quad (D3)$$

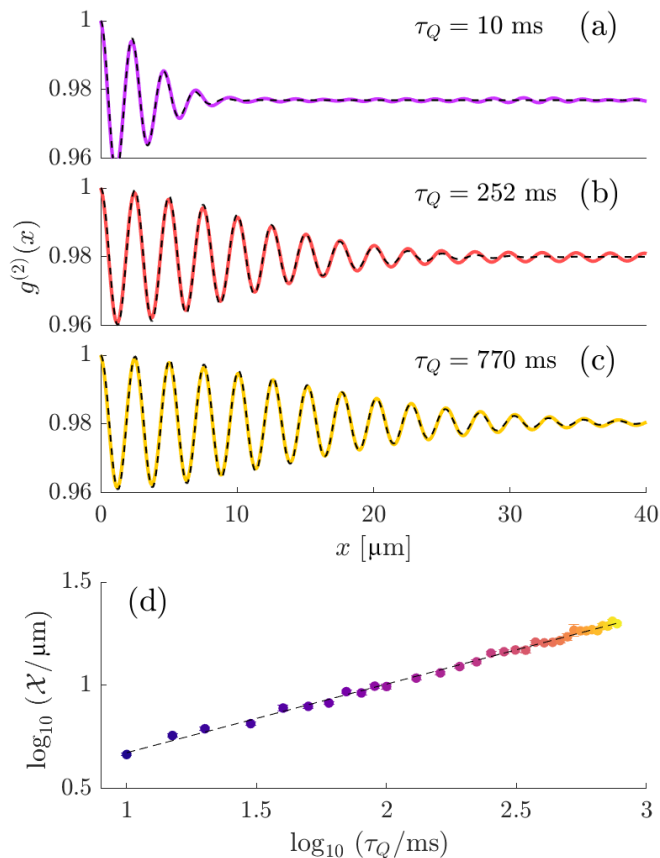


FIG. 14. Supersolid correlation length $g^{(2)}(x)$, similar to Fig. 4, now for long system sizes of 1024 unit cells, at $\tau_Q = \{10, 252, 770\}$ in panels (a)–(c), respectively. The best fit of \mathcal{X} using Eq. (8) is shown as a dashed line.

where we let $s = x - x'$ and $R = (x + x')/2$. Now, let us assume that across different trials, the supersolid wavelength is roughly the same, in other words $\langle k \rangle = \bar{k}$, $\langle k^2 \rangle = \bar{k}^2$, etc., but variations in the crystal phase $\phi(x)$ are responsible for defects in the coherent crystal. In that case, we can write

$$\begin{aligned} \langle n(x)n(x') \rangle &= \bar{n}^2 + \frac{\lambda^2}{4} [e^{2i\bar{k}R} \langle e^{i(\phi(x)+\phi(x'))} \rangle \\ &\quad + e^{i\bar{k}s} \langle e^{i(\phi(x)-\phi(x'))} \rangle + \text{H.c.}], \end{aligned} \quad (\text{D4})$$

since the exponential prefactors will not change from trial to trial. Thus,

$$\begin{aligned} \langle n(x)n(x') \rangle &= \bar{n}^2 + \frac{\lambda^2}{4} [e^{2i\bar{k}R} \langle e^{i(\phi(x)+\phi(x'))} \rangle + \text{H.c.} \\ &\quad + e^{i\bar{k}s} C^*(x-x') + e^{-i\bar{k}s} C(x-x')], \end{aligned} \quad (\text{D5})$$

$$\approx \bar{n}^2 + \frac{\lambda^2}{2} \cos(\bar{k}s) C(s), \quad (\text{D6})$$

where, in the last line, we have made the following two assumptions: (i) terms which depend on the absolute position of the phase in space, i.e., $\langle e^{i(\phi(x)+\phi(x'))} \rangle$, will average out over many trials; (ii) $C(s) = C(x-x')$ is a real-valued function that only depends on the distance $|x-x'|$. In this way, the decay of $g^{(2)}(x)$ and $C(x-x')$ appear to be related since they take a similar functional form, see Eq. (8). We

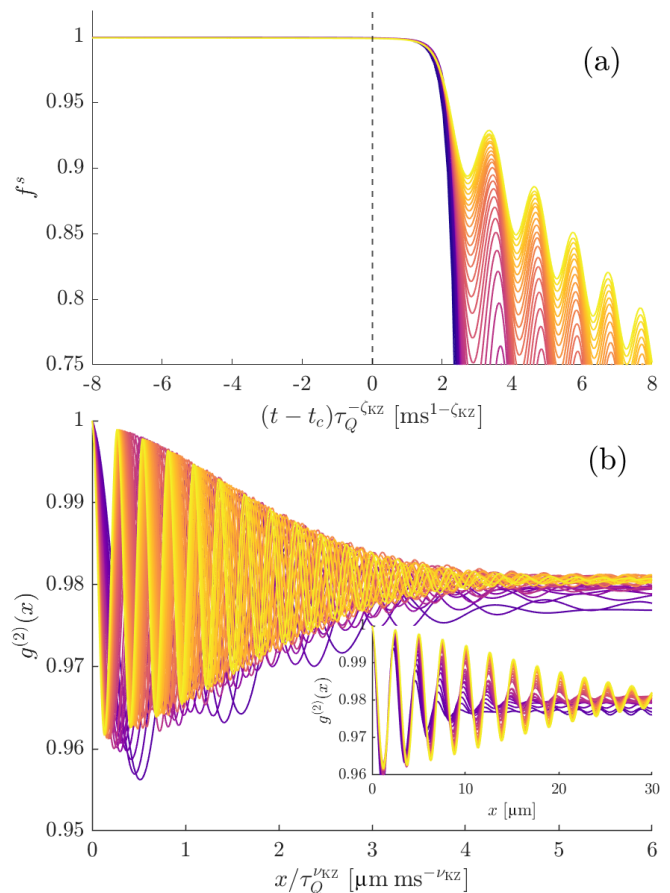


FIG. 15. Universal scaling functions. Panel (a) shows the same superfluid fraction data as in Fig. 3, now with the time domain rescaled by the extracted Kibble-Zurek exponent ζ_{KZ} , while panel (b) shows the data from Fig. 4 with the spatial domain rescaled by the extracted ν_{KZ} . While in panel (a) the full curves fall on top of one another, in panel (b) it is only the modulation envelopes that collapse to a single curve. The inset shows $g^{(2)}$ over the unscaled domain, demonstrating that the supersolid periodicity is relatively constant across different quench rates.

note that when extracting $\hat{\xi}$ from $C(x)$ in Fig. 5, we do not require $C(x-x')$ to necessarily be exponential (or Gaussian, etc.)—this is difficult to characterize due to the discrete nature of $C(x-x')$ —we are simply extracting the width at half maximum.

APPENDIX E: UNIVERSAL SCALING FUNCTIONS

In Fig. 15, we demonstrate that after determining the universal scaling exponents associated with the KZM, the observables can be collapsed to a single universal Kibble-Zurek scaling function. In particular, Fig. 15(a) shows that a rescaling of time with respect to ζ_{KZ} allows for the superfluid fraction curves to lie on top of one another, at least within the relatively early regimes we consider to be relevant for the KZM. Later, as more nonlinearities become relevant to the dynamics, there is a departure from the universal scaling function. In Fig. 15(b) there is a similar effect for the $g^{(1)}$ correlator with respect to the exponent ν_{KZ} now

plotted for all quench rates. It can be seen that rescaling the spatial domain shows that the supersolid oscillation *envelopes* scale in a universal way, but not the oscillations themselves, since the periodicity of the latter is instead set by the roton. Extremely fast quenches ($\tau_Q \lesssim 10$ ms) depart slightly from the universal envelope, likely due to large fluctuations. See

the inset of (b) for the unscaled $g^{(2)}$, where it is clear that the oscillations lie on top of one another, while the envelopes do not. Faster quenches also seem to result in a suppression of overall long-range correlations, likely due to the relatively large amount of excitations produced in the system during the quench.

-
- [1] O. Penrose and L. Onsager, Bose-Einstein condensation and liquid helium, *Phys. Rev.* **104**, 576 (1956).
- [2] E. P. Gross, Unified theory of interacting bosons, *Phys. Rev.* **106**, 161 (1957).
- [3] E. Gross, Classical theory of boson wave fields, *Ann. Phys. (NY)* **4**, 57 (1958).
- [4] A. F. Andreev and I. M. Lifshitz, Quantum theory of defects in crystals, *Zh. Eksp. Teor. Fiz.* **56**, 2057 (1969) [*Sov. Phys. JETP* **29**, 1107 (1969)].
- [5] A. J. Leggett, Can a solid be “superfluid”? *Phys. Rev. Lett.* **25**, 1543 (1970).
- [6] M. Boninsegni and N. V. Prokof'ev, *Colloquium: Supersolids: What and where are they?* *Rev. Mod. Phys.* **84**, 759 (2012).
- [7] J.-R. Li, J. Lee, W. Huang, S. Burchesky, B. Shteynas, F. Ç. Top, A. O. Jamison, and W. Ketterle, A stripe phase with supersolid properties in spin-orbit-coupled Bose-Einstein condensates, *Nature (London)* **543**, 91 (2017).
- [8] A. Putra, F. Salces-Cárcoba, Y. Yue, S. Sugawa, and I. B. Spielman, Spatial coherence of spin-orbit-coupled Bose gases, *Phys. Rev. Lett.* **124**, 053605 (2020).
- [9] L. Tanzi, E. Lucioni, F. Famà, J. Catani, A. Fioretti, C. Gabbanini, R. N. Bisset, L. Santos, and G. Modugno, Observation of a dipolar quantum gas with metastable supersolid properties, *Phys. Rev. Lett.* **122**, 130405 (2019).
- [10] F. Böttcher, J.-N. Schmidt, M. Wenzel, J. Hertkorn, M. Guo, T. Langen, and T. Pfau, Transient supersolid properties in an array of dipolar quantum droplets, *Phys. Rev. X* **9**, 011051 (2019).
- [11] L. Chomaz, D. Petter, P. Ilzhöfer, G. Natale, A. Trautmann, C. Politi, G. Durastante, R. M. W. van Bijnen, A. Patscheider, M. Sohmen, M. J. Mark, and F. Ferlaino, Long-lived and transient supersolid behaviors in dipolar quantum gases, *Phys. Rev. X* **9**, 021012 (2019).
- [12] M. Sohmen, C. Politi, L. Klaus, L. Chomaz, M. J. Mark, M. A. Norcia, and F. Ferlaino, Birth, life, and death of a dipolar supersolid, *Phys. Rev. Lett.* **126**, 233401 (2021).
- [13] T. Bland, E. Poli, C. Politi, L. Klaus, M. A. Norcia, F. Ferlaino, L. Santos, and R. N. Bisset, Two-dimensional supersolid formation in dipolar condensates, *Phys. Rev. Lett.* **128**, 195302 (2022).
- [14] S. M. Rocuzzo and F. Ancilotto, Supersolid behavior of a dipolar Bose-Einstein condensate confined in a tube, *Phys. Rev. A* **99**, 041601(R) (2019).
- [15] P. B. Blakie, D. Baillie, L. Chomaz, and F. Ferlaino, Supersolidity in an elongated dipolar condensate, *Phys. Rev. Res.* **2**, 043318 (2020).
- [16] J. C. Smith, D. Baillie, and P. B. Blakie, Supersolidity and crystallization of a dipolar Bose gas in an infinite tube, *Phys. Rev. A* **107**, 033301 (2023).
- [17] Y.-C. Zhang, F. Maucher, and T. Pohl, Supersolidity around a critical point in dipolar Bose-Einstein condensates, *Phys. Rev. Lett.* **123**, 015301 (2019).
- [18] Y.-C. Zhang, T. Pohl, and F. Maucher, Phases of supersolids in confined dipolar Bose-Einstein condensates, *Phys. Rev. A* **104**, 013310 (2021).
- [19] B. T. E. Ripley, D. Baillie, and P. B. Blakie, Two-dimensional supersolidity in a planar dipolar Bose gas, *Phys. Rev. A* **108**, 053321 (2023).
- [20] Y.-C. Zhang, T. Pohl, and F. Maucher, Metastable patterns in one- and two-component dipolar Bose-Einstein condensates, *Phys. Rev. Res.* **6**, 023023 (2024).
- [21] M. E. Fisher, Renormalization of critical exponents by hidden variables, *Phys. Rev.* **176**, 257 (1968).
- [22] G. Ódor, Universality classes in nonequilibrium lattice systems, *Rev. Mod. Phys.* **76**, 663 (2004).
- [23] J. Zinn-Justin, *Quantum Field Theory and Critical Phenomena*, 4th ed., International Series of Monographs on Physics (Clarendon Press, Oxford, England, 2002).
- [24] T. W. B. Kibble, Topology of cosmic domains and strings, *J. Phys. A: Math. Theor.* **9**, 1387 (1976).
- [25] T. W. B. Kibble, Some implications of a cosmological phase transition, *Phys. Rep.* **67**, 183 (1980).
- [26] W. H. Zurek, Cosmological experiments in superfluid helium? *Nature (London)* **317**, 505 (1985).
- [27] W. H. Zurek, Cosmological experiments in condensed matter systems, *Phys. Rep.* **276**, 177 (1996).
- [28] A. del Campo and W. H. Zurek, Universality of phase transition dynamics: Topological defects from symmetry breaking, *Int. J. Mod. Phys. A* **29**, 1430018 (2014).
- [29] T. W. B. Kibble, Phase-transition dynamics in the lab and the universe, *Phys. Today* **60**, 47 (2007).
- [30] M. Uhlmann, R. Schützhold, and U. R. Fischer, Vortex quantum creation and winding number scaling in a quenched spinor Bose gas, *Phys. Rev. Lett.* **99**, 120407 (2007).
- [31] W. H. Zurek, Causality in condensates: Gray solitons as relics of BEC formation, *Phys. Rev. Lett.* **102**, 105702 (2009).
- [32] B. Damski and W. H. Zurek, Soliton creation during a Bose-Einstein condensation, *Phys. Rev. Lett.* **104**, 160404 (2010).
- [33] A. del Campo, A. Retzker, and M. B. Plenio, The inhomogeneous Kibble-Zurek mechanism: Vortex nucleation during Bose-Einstein condensation, *New J. Phys.* **13**, 083022 (2011).
- [34] A. Das, J. Sabbatini, and W. H. Zurek, Winding up superfluid in a torus via Bose-Einstein condensation, *Sci. Rep.* **2**, 352 (2012).
- [35] A. del Campo, T. W. B. Kibble, and W. H. Zurek, Causality and non-equilibrium second-order phase transitions in inhomogeneous systems, *J. Phys.: Condens. Matter* **25**, 404210 (2013).

- [36] S.-W. Su, S.-C. Gou, A. Bradley, O. Fialko, and J. Brand, Kibble-Zurek scaling and its breakdown for spontaneous generation of Josephson vortices in Bose-Einstein condensates, *Phys. Rev. Lett.* **110**, 215302 (2013).
- [37] J. Beugnon and N. Navon, Exploring the Kibble-Zurek mechanism with homogeneous Bose gases, *J. Phys. B: At. Mol. Opt. Phys.* **50**, 022002 (2017).
- [38] S. Liu and Y. Zhang, Quench dynamics in a trapped Bose-Einstein condensate with spin-orbit coupling, *Phys. Rev. A* **99**, 053609 (2019).
- [39] P. Comaron, F. Larcher, F. Dalfovo, and N. P. Proukakis, Quench dynamics of an ultracold two-dimensional Bose gas, *Phys. Rev. A* **100**, 033618 (2019).
- [40] X. Jiang, S. Wu, Q. Ye, and C. Lee, Universality of miscible-immiscible phase separation dynamics in two-component Bose-Einstein condensates, *New J. Phys.* **21**, 023014 (2019).
- [41] I.-K. Liu, J. Dziarmaga, S.-C. Gou, F. Dalfovo, and N. P. Proukakis, Kibble-Zurek dynamics in a trapped ultracold Bose gas, *Phys. Rev. Res.* **2**, 033183 (2020).
- [42] M. Thudiyangal and A. del Campo, Universal vortex statistics and stochastic geometry of Bose-Einstein condensation, *Phys. Rev. Res.* **6**, 033152 (2024).
- [43] N. P. Proukakis, Universality of Bose-Einstein condensation and quenched formation dynamics, in *Encyclopedia of Condensed Matter Physics*, 2nd. ed., edited by T. Chakraborty (Academic Press, Oxford, 2024), pp. 84–123.
- [44] M. T. Wheeler, H. Salman, and M. O. Borgh, Dynamics of a nonequilibrium discontinuous quantum phase transition in a spinor Bose-Einstein condensate, *Commun. Phys.* **8**, 153 (2025).
- [45] C. N. Weiler, T. W. Neely, D. R. Scherer, A. S. Bradley, M. J. Davis, and B. P. Anderson, Spontaneous vortices in the formation of Bose-Einstein condensates, *Nature (London)* **455**, 948 (2008).
- [46] G. Lamporesi, S. Donadello, S. Serafini, F. Dalfovo, and G. Ferrari, Spontaneous creation of Kibble-Zurek solitons in a Bose-Einstein condensate, *Nat. Phys.* **9**, 656 (2013).
- [47] L. Corman, L. Chomaz, T. Bienaimé, R. Desbuquois, C. Weitenberg, S. Nascimbène, J. Dalibard, and J. Beugnon, Quench-induced supercurrents in an annular Bose gas, *Phys. Rev. Lett.* **113**, 135302 (2014).
- [48] N. Navon, A. L. Gaunt, R. P. Smith, and Z. Hadzibabic, Critical dynamics of spontaneous symmetry breaking in a homogeneous Bose gas, *Science* **347**, 167 (2015).
- [49] L. Chomaz, L. Corman, T. Bienaimé, R. Desbuquois, C. Weitenberg, S. Nascimbène, J. Beugnon, and J. Dalibard, Emergence of coherence via transverse condensation in a uniform quasi-two-dimensional Bose gas, *Nat. Commun.* **6**, 6162 (2015).
- [50] S. Donadello, S. Serafini, T. Bienaimé, F. Dalfovo, G. Lamporesi, and G. Ferrari, Creation and counting of defects in a temperature-quenched Bose-Einstein condensate, *Phys. Rev. A* **94**, 023628 (2016).
- [51] L. W. Clark, L. Feng, and C. Chin, Universal space-time scaling symmetry in the dynamics of bosons across a quantum phase transition, *Science* **354**, 606 (2016).
- [52] I. K. Liu, S. Donadello, G. Lamporesi, G. Ferrari, S. C. Gou, F. Dalfovo, and N. P. Proukakis, Dynamical equilibration across a quenched phase transition in a trapped quantum gas, *Commun. Phys.* **1**, 24 (2018).
- [53] B. Ko, J. W. Park, and Y. Shin, Kibble-Zurek universality in a strongly interacting Fermi superfluid, *Nat. Phys.* **15**, 1227 (2019).
- [54] J. Goo, Y. Lim, and Y. Shin, Defect saturation in a rapidly quenched Bose gas, *Phys. Rev. Lett.* **127**, 115701 (2021).
- [55] X.-P. Liu, X.-C. Yao, Y. Deng, Y.-X. Wang, X.-Q. Wang, X. Li, Q. Chen, Y.-A. Chen, and J.-W. Pan, Dynamic formation of quasicondensate and spontaneous vortices in a strongly interacting Fermi gas, *Phys. Rev. Res.* **3**, 043115 (2021).
- [56] J. Goo, Y. Lee, Y. Lim, D. Bae, T. Rabga, and Y. Shin, Universal early coarsening of quenched Bose gases, *Phys. Rev. Lett.* **128**, 135701 (2022).
- [57] T. Rabga, Y. Lee, D. Bae, M. Kim, and Y. Shin, Variations of the Kibble-Zurek scaling exponents of trapped Bose gases, *Phys. Rev. A* **108**, 023315 (2023).
- [58] D. G. Allman, P. Sabharwal, and K. C. Wright, Quench-induced spontaneous currents in rings of ultracold fermionic atoms, *Phys. Rev. A* **109**, 053320 (2024).
- [59] W. H. Zurek, U. Dorner, and P. Zoller, Dynamics of a quantum phase transition, *Phys. Rev. Lett.* **95**, 105701 (2005).
- [60] A. Polkovnikov, Universal adiabatic dynamics in the vicinity of a quantum critical point, *Phys. Rev. B* **72**, 161201(R) (2005).
- [61] L. E. Sadler, J. M. Higbie, S. R. Leslie, M. Vengalattore, and D. M. Stamper-Kurn, Spontaneous symmetry breaking in a quenched ferromagnetic spinor Bose-Einstein condensate, *Nature (London)* **443**, 312 (2006).
- [62] D. Chen, M. White, C. Borries, and B. DeMarco, Quantum quench of an atomic Mott insulator, *Phys. Rev. Lett.* **106**, 235304 (2011).
- [63] M. Anquez, B. A. Robbins, H. M. Bharath, M. Boguslawski, T. M. Hoang, and M. S. Chapman, Quantum Kibble-Zurek mechanism in a spin-1 Bose-Einstein condensate, *Phys. Rev. Lett.* **116**, 155301 (2016).
- [64] L. Feng, L. W. Clark, A. Gaj, and C. Chin, Coherent inflationary dynamics for Bose-Einstein condensates crossing a quantum critical point, *Nat. Phys.* **14**, 269 (2018).
- [65] Y. Chen, M. Horikoshi, K. Yoshioka, and M. Kuwata-Gonokami, Dynamical critical behavior of an attractive Bose-Einstein condensate phase transition, *Phys. Rev. Lett.* **122**, 040406 (2019).
- [66] C.-R. Yi, S. Liu, R.-H. Jiao, J.-Y. Zhang, Y.-S. Zhang, and S. Chen, Exploring inhomogeneous Kibble-Zurek mechanism in a spin-orbit coupled Bose-Einstein condensate, *Phys. Rev. Lett.* **125**, 260603 (2020).
- [67] K. Lee, S. Kim, T. Kim, and Y. Shin, Universal Kibble-Zurek scaling in an atomic Fermi superfluid, *Nat. Phys.* **20**, 1570 (2024).
- [68] I. Ferrier-Barbut, H. Kadau, M. Schmitt, M. Wenzel, and T. Pfau, Observation of quantum droplets in a strongly dipolar Bose gas, *Phys. Rev. Lett.* **116**, 215301 (2016).
- [69] F. Wächtler and L. Santos, Quantum filaments in dipolar Bose-Einstein condensates, *Phys. Rev. A* **93**, 061603(R) (2016).
- [70] L. Chomaz, S. Baier, D. Petter, M. J. Mark, F. Wächtler, L. Santos, and F. Ferlaino, Quantum-fluctuation-driven crossover from a dilute Bose-Einstein condensate to a macrodroplet in a dipolar quantum fluid, *Phys. Rev. X* **6**, 041039 (2016).
- [71] R. Schützhold, M. Uhlmann, Y. Xu, and U. R. Fischer, Mean-field expansion in Bose-Einstein condensates with finite-range interactions, *Int. J. Mod. Phys. B* **20**, 3555 (2006).

- [72] A. R. P. Lima and A. Pelster, Quantum fluctuations in dipolar Bose gases, *Phys. Rev. A* **84**, 041604(R) (2011).
- [73] P. B. Blakie, D. Baillie, and S. Pal, Variational theory for the ground state and collective excitations of an elongated dipolar condensate, *Commun. Theor. Phys.* **72**, 085501 (2020).
- [74] S. Pal, D. Baillie, and P. B. Blakie, Excitations and number fluctuations in an elongated dipolar Bose-Einstein condensate, *Phys. Rev. A* **102**, 043306 (2020).
- [75] P. B. Blakie, L. Chomaz, D. Baillie, and F. Ferlaino, Compressibility and speeds of sound across the superfluid-to-supersolid phase transition of an elongated dipolar gas, *Phys. Rev. Res.* **5**, 033161 (2023).
- [76] A. J. Leggett, On the superfluid fraction of an arbitrary many-body system at $T = 0$, *J. Stat. Phys.* **93**, 927 (1998).
- [77] A. Alaña, N. Antolini, G. Biagioni, I. L. Egusquiza, and M. Modugno, Crossing the superfluid-supersolid transition of an elongated dipolar condensate, *Phys. Rev. A* **106**, 043313 (2022).
- [78] G. Biagioni, N. Antolini, A. Alaña, M. Modugno, A. Fioretti, C. Gabbanini, L. Tanzi, and G. Modugno, Dimensional crossover in the superfluid-supersolid quantum phase transition, *Phys. Rev. X* **12**, 021019 (2022).
- [79] P. Blakie, A. Bradley, M. Davis, R. Ballagh, and C. Gardiner, Dynamics and statistical mechanics of ultra-cold Bose gases using c-field techniques, *Adv. Phys.* **57**, 363 (2008).
- [80] A. Alaña, I. L. Egusquiza, and M. Modugno, Supersolid formation in a dipolar condensate by roton instability, *Phys. Rev. A* **108**, 033316 (2023).
- [81] A. Alaña, Supersolid-formation-time shortcut and excitation reduction by manipulating the dynamical instability, *Phys. Rev. A* **109**, 023308 (2024).
- [82] J. Sabbatini, W. H. Zurek, and M. J. Davis, Phase separation and pattern formation in a binary Bose-Einstein condensate, *Phys. Rev. Lett.* **107**, 230402 (2011).
- [83] L. Pitaevskii and S. Stringari, *Bose-Einstein Condensation and Superfluidity* (Oxford University Press, Oxford, 2016).
- [84] K. Roychowdhury, R. Moessner, and A. Das, Dynamics and correlations at a quantum phase transition beyond Kibble-Zurek, *Phys. Rev. B* **104**, 014406 (2021).
- [85] R. J. Nowak and J. Dziarmaga, Quantum Kibble-Zurek mechanism: Kink correlations after a quench in the quantum Ising chain, *Phys. Rev. B* **104**, 075448 (2021).
- [86] H.-C. Kou and P. Li, Interferometry based on the quantum Kibble-Zurek mechanism, *Phys. Rev. B* **106**, 184301 (2022).
- [87] H.-C. Kou and P. Li, Varying quench dynamics in the transverse Ising chain: The Kibble-Zurek, saturated, and pre-saturated regimes, *Phys. Rev. B* **108**, 214307 (2023).
- [88] A. Bray, Theory of phase-ordering kinetics, *Adv. Phys.* **43**, 357 (1994).
- [89] M. Uhlmann, R. Schützhold, and U. R. Fischer, $O(N)$ symmetry-breaking quantum quench: Topological defects versus quasiparticles, *Phys. Rev. D* **81**, 025017 (2010).
- [90] M. Uhlmann, R. Schützhold, and U. R. Fischer, System size scaling of topological defect creation in a second-order dynamical quantum phase transition, *New J. Phys.* **12**, 095020 (2010).
- [91] T. Bland, Q. Marolleau, P. Comaron, B. Malomed, and N. Proukakis, Persistent current formation in double-ring geometries, *J. Phys. B: At. Mol. Opt. Phys.* **53**, 115301 (2020).
- [92] H.-B. Zeng, C.-Y. Xia, and A. del Campo, Universal breakdown of Kibble-Zurek scaling in fast quenches across a phase transition, *Phys. Rev. Lett.* **130**, 060402 (2023).
- [93] A. del Campo, F. J. Gómez-Ruiz, Z.-H. Li, C.-Y. Xia, H.-B. Zeng, and H.-Q. Zhang, Universal statistics of vortices in a newborn holographic superconductor: Beyond the Kibble-Zurek mechanism, *J. High Energy Phys.* **06** (2021) 061.
- [94] F. Balducci, M. Beau, J. Yang, A. Gambassi, and A. del Campo, Large deviations beyond the Kibble-Zurek mechanism, *Phys. Rev. Lett.* **131**, 230401 (2023).
- [95] A. del Campo, Universal statistics of topological defects formed in a quantum phase transition, *Phys. Rev. Lett.* **121**, 200601 (2018).
- [96] F. J. Gómez-Ruiz, J. J. Mayo, and A. del Campo, Full counting statistics of topological defects after crossing a phase transition, *Phys. Rev. Lett.* **124**, 240602 (2020).
- [97] J.-M. Cui, F. J. Gómez-Ruiz, Y.-F. Huang, C.-F. Li, G.-C. Guo, and A. del Campo, Experimentally testing quantum critical dynamics beyond the Kibble-Zurek mechanism, *Commun. Phys.* **3**, 44 (2020).
- [98] Y. Bando, Y. Susa, H. Oshiyama, N. Shibata, M. Ohzeki, F. J. Gómez-Ruiz, D. A. Lidar, S. Suzuki, A. del Campo, and H. Nishimori, Probing the universality of topological defect formation in a quantum annealer: Kibble-Zurek mechanism and beyond, *Phys. Rev. Res.* **2**, 033369 (2020).
- [99] S. Sachdev, *Quantum Phase Transitions*, 2nd ed. (Cambridge University Press, Cambridge, 2011).
- [100] P. C. Hohenberg and B. I. Halperin, Theory of dynamic critical phenomena, *Rev. Mod. Phys.* **49**, 435 (1977).
- [101] M. J. Steel, M. K. Olsen, L. I. Plimak, P. D. Drummond, S. M. Tan, M. J. Collett, D. F. Walls, and R. Graham, Dynamical quantum noise in trapped Bose-Einstein condensates, *Phys. Rev. A* **58**, 4824 (1998).
- [102] A. Sinatra, C. Lobo, and Y. Castin, The truncated Wigner method for Bose-condensed gases: limits of validity and applications, *J. Phys. B: At. Mol. Opt. Phys.* **35**, 3599 (2002).
- [103] A. Jelić and L. F. Cugliandolo, Quench dynamics of the 2d XY model, *J. Stat. Mech.* (2011) P02032.
- [104] J. Dziarmaga and W. H. Zurek, Quench in the 1D Bose-Hubbard model: Topological defects and excitations from the Kosterlitz-Thouless phase transition dynamics, *Sci. Rep.* **4**, 5950 (2014).
- [105] B. Gardas, J. Dziarmaga, and W. H. Zurek, Dynamics of the quantum phase transition in the one-dimensional Bose-Hubbard model: Excitations and correlations induced by a quench, *Phys. Rev. B* **95**, 104306 (2017).
- [106] Z. Zuo, S. Yin, X. Cao, and F. Zhong, Scaling theory of the Kosterlitz-Thouless phase transition, *Phys. Rev. B* **104**, 214108 (2021).
- [107] M. P. A. Fisher, P. B. Weichman, G. Grinstein, and D. S. Fisher, Boson localization and the superfluid-insulator transition, *Phys. Rev. B* **40**, 546 (1989).
- [108] Q. Huang, R. Yao, L. Liang, S. Wang, Q. Zheng, D. Li, W. Xiong, X. Zhou, W. Chen, X. Chen, and J. Hu, Observation of many-body quantum phase transitions beyond the Kibble-Zurek mechanism, *Phys. Rev. Lett.* **127**, 200601 (2021).
- [109] A. van Otterlo, K.-H. Wagenblast, R. Baltin, C. Bruder, R. Fazio, and G. Schön, Quantum phase transitions of interacting bosons and the supersolid phase, *Phys. Rev. B* **52**, 16176 (1995).

- [110] F. Bloch, Superfluidity in a ring, *Phys. Rev. A* **7**, 2187 (1973).
- [111] L. Amico, A. Osterloh, and F. Cataliotti, Quantum many particle systems in ring-shaped optical lattices, *Phys. Rev. Lett.* **95**, 063201 (2005).
- [112] L. Amico, D. Anderson, M. Boshier, J.-P. Brantut, L.-C. Kwek, A. Minguzzi, and W. von Klitzing, *Colloquium: Atomtronic circuits: From many-body physics to quantum technologies*, *Rev. Mod. Phys.* **94**, 041001 (2022).
- [113] C. Ryu, M. F. Andersen, P. Cladé, V. Natarajan, K. Helmerson, and W. D. Phillips, Observation of persistent flow of a Bose-Einstein condensate in a toroidal trap, *Phys. Rev. Lett.* **99**, 260401 (2007).
- [114] A. Ramanathan, K. C. Wright, S. R. Muniz, M. Zelan, W. T. Hill, C. J. Lobb, K. Helmerson, W. D. Phillips, and G. K. Campbell, Superflow in a toroidal Bose-Einstein condensate: An atom circuit with a tunable weak link, *Phys. Rev. Lett.* **106**, 130401 (2011).
- [115] K. C. Wright, R. B. Blakestad, C. J. Lobb, W. D. Phillips, and G. K. Campbell, Driving phase slips in a superfluid atom circuit with a rotating weak link, *Phys. Rev. Lett.* **110**, 025302 (2013).
- [116] S. Eckel, J. G. Lee, F. Jendrzejewski, N. Murray, C. W. Clark, C. J. Lobb, W. D. Phillips, M. Edwards, and G. K. Campbell, Hysteresis in a quantized superfluid ‘atomtronic’ circuit, *Nature (London)* **506**, 200 (2014).
- [117] K. Henderson, C. Ryu, C. MacCormick, and M. G. Boshier, Experimental demonstration of painting arbitrary and dynamic potentials for Bose-Einstein condensates, *New J. Phys.* **11**, 043030 (2009).
- [118] B. E. Sherlock, M. Gildemeister, E. Owen, E. Nugent, and C. J. Foot, Time-averaged adiabatic ring potential for ultracold atoms, *Phys. Rev. A* **83**, 043408 (2011).
- [119] S. Moulder, S. Beattie, R. P. Smith, N. Tammuz, and Z. Hadzibabic, Quantized supercurrent decay in an annular Bose-Einstein condensate, *Phys. Rev. A* **86**, 013629 (2012).
- [120] C. Ryu, P. W. Blackburn, A. A. Blinova, and M. G. Boshier, Experimental realization of Josephson junctions for an atom squid, *Phys. Rev. Lett.* **111**, 205301 (2013).
- [121] S. Beattie, S. Moulder, R. J. Fletcher, and Z. Hadzibabic, Persistent currents in spinor condensates, *Phys. Rev. Lett.* **110**, 025301 (2013).
- [122] G. E. Marti, R. Olf, and D. M. Stamper-Kurn, Collective excitation interferometry with a toroidal Bose-Einstein condensate, *Phys. Rev. A* **91**, 013602 (2015).
- [123] M. N. Tengstrand, D. Boholm, R. Sachdeva, J. Bengtsson, and S. M. Reimann, Persistent currents in toroidal dipolar supersolids, *Phys. Rev. A* **103**, 013313 (2021).
- [124] M. N. Tengstrand, P. Stürmer, J. Ribbing, and S. M. Reimann, Toroidal dipolar supersolid with a rotating weak link, *Phys. Rev. A* **107**, 063316 (2023).
- [125] V. Mukherjee, A. Dutta, and D. Sen, Defect generation in a spin- $\frac{1}{2}$ transverse XY chain under repeated quenching of the transverse field, *Phys. Rev. B* **77**, 214427 (2008).
- [126] U. Divakaran and A. Dutta, Reverse quenching in a one-dimensional Kitaev model, *Phys. Rev. B* **79**, 224408 (2009).
- [127] H. T. Quan and W. H. Zurek, Testing quantum adiabaticity with quench echo, *New J. Phys.* **12**, 093025 (2010).